

Subharmonic Control of a Fluxonium Qubit via a Purcell-Protected Flux Line

J. Schirk^{1,2,*} F. Wallner^{1,2,*} L. Huang^{1,2} I. Tsitsilin^{1,2} N. Bruckmoser^{1,2} L. Koch^{1,2}
 D. Bunch^{1,2} N.J. Glaser^{1,2} G.B.P. Huber^{1,2} M. Knudsen^{1,2} G. Krylov^{1,2} A. Marx,²
 F. Pfeiffer^{1,2} L. Richard^{1,2} F.A. Roy^{2,3} J.H. Romeiro^{1,2} M. Singh,^{1,2} L. Södergren^{1,2}
 E. Dionis,⁴ D. Sugny⁴ M. Werninghaus^{1,2} K. Liegener^{1,2} C.M.F. Schneider^{1,2,†}
 and S. Filipp^{1,2,5}

¹Department of Physics, *Technical University of Munich, TUM School of Natural Sciences*,
 85748 Garching, Germany

²Walther-Meißner-Institut, *Bayerische Akademie der Wissenschaften*, 85748 Garching, Germany

³Theoretical Physics, *Saarland University*, 66123 Saarbrücken, Germany

⁴Laboratoire Interdisciplinaire Carnot de Bourgogne (ICB), UMR 6303 CNRS—*Université de Bourgogne*,
 9 Av. A. Savary, BP 47 870, F-21078 Dijon, France

⁵Munich Center for Quantum Science and Technology (MCQST), 80799 München, Germany



(Received 31 October 2024; revised 28 May 2025; accepted 24 June 2025; published 29 July 2025)

Protecting qubits from environmental noise while maintaining strong coupling for fast high-fidelity control is a central challenge for quantum information processing. Here, we demonstrate a control scheme for superconducting fluxonium qubits that eliminates qubit decay through the control channel by suppressing the environmental density of states at the transition frequency. Adding a low-pass filter on the flux line allows for flux-biasing and, at the same time, coherently controlling the fluxonium qubit by parametrically driving it at integer fractions of its transition frequency. We compare the filtered to the unfiltered configuration and find a 5-times-longer T_1 , and a 10-times-improved T_2 -echo time in the filtered case. We demonstrate coherent control with up to 11-photon subharmonic drives, highlighting the strong nonlinearity of the fluxonium potential. Measured Rabi frequencies and drive-induced frequency shifts show excellent agreement with numerical and analytical models. Furthermore, we show the equivalence of a 3-photon subharmonic drive to an on-resonance drive by benchmarking subharmonic gate fidelities above 99.94%. These results open up a scalable path for full qubit control through a single Purcell-protected channel, providing strong suppression of control-induced decoherence and enabling wiring-efficient superconducting quantum processors.

DOI: [10.1103/yn15-jyl7](https://doi.org/10.1103/yn15-jyl7)

I. INTRODUCTION

Superconducting circuits are a promising platform for scalable error-corrected quantum processors [1–3]. This potential has been enabled by collective efforts in improving circuits based on transmon qubits [4], culminating in demonstrating quantum algorithms close to practical utility [5]. One of the main limitations for current superconducting quantum processors is decoherence [2], which sets an upper bound on achievable gate fidelities. To

improve further, it is crucial to understand, characterize, and close all channels contributing to the loss of quantum information [6,7].

Decoherence channels can be classified into two categories: internal and external losses [8]. Internal losses arise from material imperfections such as two-level systems (TLSs) that couple to the qubit [6,9,10]. By optimizing designs and fabrication processes, it is possible to significantly reduce both the coupling to TLSs and their density [11,12]. In this regard, the fluxonium qubit [13,14] stands out, demonstrating record-high coherence times [13,15,16] among superconducting qubits, attributed to its weaker coupling to TLSs at low transition frequencies of a few hundred megahertz [17]. Recently, the single-qubit and two-qubit gate performance of fluxonium qubits [16,18,19] has surpassed that of the more widely used transmon qubits, thus providing a viable alternative for superconducting quantum processors [20].

*These authors contributed equally to this work.

†Contact author: christian.schneider@wmi.badw.de

Published by the American Physical Society under the terms of the *Creative Commons Attribution 4.0 International* license. Further distribution of this work must maintain attribution to the author(s) and the published article's title, journal citation, and DOI.

External sources of decoherence result from signal lines that are required to control the qubits [21–24]. One approach to mitigate their impact is to reduce the coupling between the qubit and the control lines, while compensating with increased drive power. However, this strategy is ultimately constrained by the limited cooling power available in state-of-the-art cryogenic systems [23]. As a result, fast and high-fidelity control necessitates a finite sufficiently strong coupling to a control line [25]. However, since linear couplings are reciprocal, the control line inevitably acts as a decay channel for the qubit. Ideally, one would like to independently engineer the coupling for qubit control from the qubit dissipation into the control channel [25]. Breaking the reciprocity of these processes requires exploiting nonlinear effects such as multiphoton processes, which are observed in nonlinear media where driven systems interact with higher harmonics [26–28], or with subharmonics at integer fractions of the transition frequency [29–34]. Fluxonium qubits, with their strong nonlinear potential, are well suited for multiphoton control processes. Interestingly, such multiphoton processes can be driven directly via an inductively coupled flux-bias line. This same line serves to maintain the fluxonium at its ideal operation point, where it is first-order insensitive to flux noise. In addition to minimizing the number of control elements, resonant flux control has been shown to yield higher single-qubit-gate fidelities than charge-based control in fluxonium qubits, making it especially attractive for implementing multiphoton gates [35]. To suppress noise at the qubit transition frequency and reduce decoherence introduced by the control line, a low-pass filter can be inserted into the flux line. In this configuration, subharmonic control enables full qubit control over a single filtered channel, eliminating the need to resonantly drive the qubit at its transition frequency over a separate charge line.

In this work, we demonstrate subharmonic control of a fluxonium qubit using a control channel with a low-pass filter below the fundamental qubit frequency. We confirm that the low-pass filter isolates the qubit from external noise when idling, resulting in a fluxonium primarily limited by internal losses and readout-resonator population. Subsequently, we demonstrate coherent control of the fluxonium qubit through the filtered channel using subharmonic driving. This results in single-qubit gates with fidelities above $\mathcal{F} > 99.9\%$.

II. PURCELL PROTECTION

Qubit dissipation into its environment is described by Fermi's golden rule. For an environment with power spectral density $S(\omega)$ coupling to the qubit via the transition operator \hat{A} , the relaxation rate γ_{eg} between the qubit ground

state $|g\rangle$ and the first excited state $|e\rangle$ is given by [4,22,36]

$$\gamma_{\text{eg}} = \frac{1}{\hbar^2} |\langle g|\hat{A}|e\rangle|^2 S(\omega_{\text{eg}}), \quad (1)$$

where $\hbar\omega_{\text{eg}}$ is the energy separation of the qubit states. The power spectral density of an environment inductively coupled to a superconducting circuit is given by the fluctuation-dissipation theorem [36,37],

$$S(\omega) = \hbar\omega \frac{R(\omega)}{|Z(\omega)|^2} \left[1 + \coth\left(\frac{\hbar\omega}{2k_B T}\right) \right]. \quad (2)$$

Here, the first term describes spontaneous emission and the second term induced emission and absorption processes. We model the environment without loss of generality as a parallel-current noise source with impedance $Z(\omega)$. Similarly, the environment can be modeled as a parallel-noise voltage source with capacitive coupling [21, 38]. The impedance consists of a resistive component $R(\omega) = \text{Re}[Z(\omega)]$ at temperature T and reactive components $X(\omega) = \text{Im}[Z(\omega)]$. The latter can be composed of inductive and capacitive elements, leading to a frequency-dependent reactance and, therefore, a filter transfer function.

According to Eq. (1), qubit dissipation is suppressed when the matrix element $\langle g|\hat{A}|e\rangle$ vanishes, as is the case in protected circuits such as the zero-pi [39] or inductively shunted transmon [40]. In circuits with nonvanishing matrix elements, qubit dissipation can instead be reduced by lowering the noise spectral density $S(\omega_{\text{eg}})$ according to Eq. (2). This reduction can be achieved by lowering the temperature, since the coth term approaches unity for $T \rightarrow 0$, minimizing stimulated emission. This is typically achieved in qubits with transition frequencies above 5 GHz by state-of-the-art dilution cryostats at millikelvin temperatures [23]. For fluxonium qubits with transition frequencies below 1 GHz, this approximation is no longer valid due to the exponential increase of the coth term for $\hbar\omega/2k_B T < 1$.

However, the inclusion of reactive elements offers another possibility to suppress environment-induced qubit relaxation by modifying the complex impedance $Z(\omega)$ at the qubit frequency ω_{eg} . This approach affects both the stimulated- and spontaneous-emission terms in Eq. (2) and is referred to as Purcell protection [41]. We can achieve a vanishing power spectral density at the qubit frequency $S(\omega_{\text{eg}}) \rightarrow 0$ by either $R(\omega_{\text{eg}}) \rightarrow 0$ for finite $|Z(\omega_{\text{eg}})|$ or $|Z(\omega_{\text{eg}})| \rightarrow \infty$ for finite $R(\omega_{\text{eg}})$. The former describes a low-pass filter above the cutoff frequency and the latter a high-pass filter below the cutoff frequency. As fluxonium qubits require a dc bias for their ideal operation point, we will focus on low-pass filters in the following. Intuitively, the reduction of the decay rate for low-pass filters occurs because a vanishing resistance results in smaller fluctuations according to the fluctuation-dissipation theorem.

While a low-pass filter below the qubit frequency ω_{eg} results in a vanishing contribution of the control line to γ_{eg} , it prevents direct driving of the qubit at $\omega_d = \omega_{\text{eg}}$. However, through subharmonic control, as described below in Sec. III, we decrease the drive frequency ω_d to a regime well below the cutoff frequency of the filter, restoring qubit control capabilities while retaining low qubit dissipation.

We first demonstrate the suppression of qubit dissipation through filtering at the qubit frequency on a fluxonium qubit consisting of a single junction with Josephson energy E_J , shunted by capacitive pads with a charging energy E_C and an inductance with inductive energy E_L , as shown in Fig. 1(a). The fluxonium circuit is described by the Hamiltonian [42]

$$\hat{H} = 4E_C \hat{n}^2 - E_J \cos \hat{\phi} + \frac{E_L}{2} [\hat{\phi} - \phi(t)]^2, \quad (3)$$

with the reduced phase and charge operators $\hat{\phi}$, \hat{n} and the external flux $\phi(t) = 2\pi \Phi(t)/\Phi_0$ in units of the magnetic flux quantum Φ_0 . A false-color micrograph of the device is shown in Fig. 1(b) and further details of the circuit and its parameters are listed in Appendix A. We include both an inductively coupled flux line to control the external flux and the qubit states as well as an auxiliary weakly coupled microwave (MW) line as a reference for controlling the qubit states. The flux line couples to the fluxonium via the phase operator $\hat{\phi}$ and the MW line via the charge operator \hat{n} . Since the MW line is only weakly coupled and is strongly attenuated, we neglect it in the following discussion.

In order to modify the impedance of the flux line, we insert a low-pass filter (Minicircuits VLFX780+) with a 3-dB cutoff frequency at 950 MHz, which is well below the qubit frequency $\omega_{\text{eg}}/2\pi = 1.32$ GHz [Fig. 1(c)]. The filter decreases $R(\omega_{\text{eg}})/|Z(\omega_{\text{eg}})|^2$ to reduce relaxation according to Eq. (2). Below the cutoff frequency, it is maintained at $R(\omega_{\text{eg}})/|Z(\omega_{\text{eg}})|^2 \approx 1/50 \Omega$ to enable fast control operations. To assess the effect of the filtered environment on qubit performance, we excite the qubit resonantly over the MW line and measure the relaxation (T_1), the Ramsey coherence (T_2^*), and the Hahn-echo times (T_2^e) of the fluxonium qubit separately for the unfiltered (UF) and low-pass-filtered (LP) flux-line configurations. Our setup includes a cryogenic microwave switch [Fig. 1(a)], to change *in situ* between both configurations. We measure the coherence times in both configurations for several hours. The results are plotted as integrated histograms in Fig. 1(d), with the median values depicted in Table I. Adding the filter significantly increases average relaxation times by a factor of 5, up to $T_1 = 168(20) \mu\text{s}$, and dephasing times by a factor of 3 and of 10, up to $T_2^* = 75(9) \mu\text{s}$ and $T_2^e = 223(37) \mu\text{s}$, respectively.

In addition, we extract the effective qubit temperature T_{eff} from single-shot measurements (for details, see

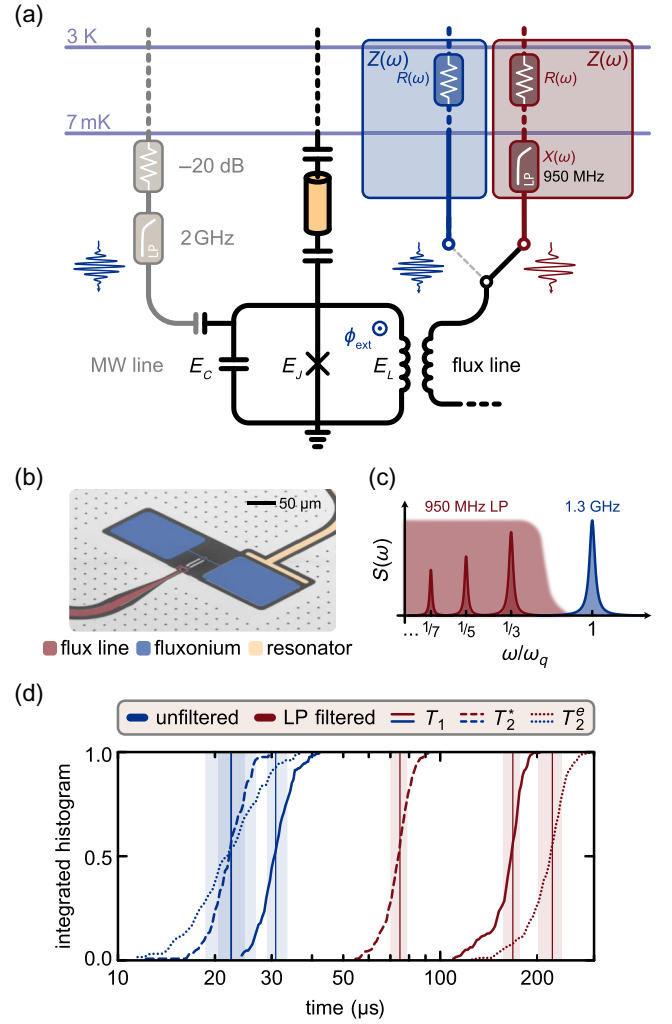


FIG. 1. The setup and the relaxation times. (a) The setup at the low-temperature stages of the cryostat (the 1-K and 100-mK stages are left out and are displayed in Appendix 6), including the readout resonator and two switchable flux-line configurations [unfiltered (UF) and low-pass filtered (LP)]. An additional microwave (MW) line is added for comparison and benchmarking. (b) A false-color micrograph of the fluxonium (blue) with a galvanically coupled flux line (red) and a capacitively coupled readout resonator (yellow). The additional MW line is located outside of the micrograph cut-out shown here. (c) A sketch of the power spectral density $S(\omega)$ for the resonant (blue) and subharmonic drive (red) setups. The shaded area indicates the pass band of the low-pass filter. (d) Integrated histograms for the T_1 (solid), T_2^* (dashed), and T_2^e (dotted) for unfiltered (blue) and filtered (red) flux-line configurations. The vertical lines with shaded areas illustrate the median and standard deviation, with values given in Table I.

Appendix D). We observe a decrease in the effective temperature from $T_{\text{eff}} = 245(25)$ mK without the LP filter (UF) to $T_{\text{eff}} = 28.9(5)$ mK with the filter (LP). These results confirm that the relaxation time for the unfiltered-line setup is dominantly limited by stimulated emission

TABLE I. The decoherence times and the effective qubit temperature for the filtered and unfiltered setups. The energy relaxation T_1 , the Ramsey coherence T_2^* , the Hahn echo T_2^e , and the effective temperature T_{eff} are listed for the unfiltered and low-pass-filtered flux-line configurations.

	Unfiltered	LP filtered	Improvement
T_1	31(5) μs	168(20) μs	$\times 5$ (1)
T_2^*	22(4) μs	75(9) μs	$\times 3$ (1)
T_2^e	22(8) μs	223(37) μs	$\times 10$ (4)
T_{eff}	245(25) mK	28(1) mK	$\times 9$ (1)

due to thermal photons, with $T_1 \propto 1/(2n_{\text{th}} + 1)$ [43]. For further verification, we extract the coupling of the qubit to the flux line, represented as a bath at different temperatures. With the measured power transmission factor of approximately -35.5 dB for the low-pass filter at ω_{eg} and assuming that the lowest-temperature attenuator of the flux line is well thermalized to 3 K, we determine a coupling rate of $\gamma_{\text{flux}} = 1/3.6(5)$ ms for the flux line, as detailed in Appendix D. This value agrees well with the design value of $\gamma_{\text{flux}} = 1/3.4$ ms.

Furthermore, in the unfiltered configuration, we observe almost equal values for the Ramsey coherence T_2^* and Hahn-echo times T_2^e . This suggests that high-frequency noise is the dominant source for decoherence in this configuration, since it cannot be compensated by the low-frequency-noise-insensitive Hahn-echo sequence. In the low-pass-filtered case, we observe a large difference between T_2^e and T_2^* , pointing toward low-frequency noise as the primary decoherence mechanism [44]. Given that the fluxonium qubit is first-order insensitive to flux noise at its sweet spot, we attribute the observed dephasing primarily to thermal photons in the readout resonator. By using a dispersive model for the qubit-resonator system described in Appendix C, we estimate an effective resonator temperature of 51(1) mK, which is in good agreement with temperatures reported in other works [13,45–47]. This indicates that coherence is not limited by flux noise through the passband of the low-pass filter but, rather, by the strong coupling between the readout resonator and the qubit.

III. PARAMETRIC SUBHARMONIC DRIVING

While filtering is an effective method to protect the idling qubit from relaxation caused by control lines, it impedes control over the qubit state using drive pulses at its transition frequency ω_{eg} . This limitation is overcome by driving the qubit at an integer fraction ω_{eg}/n of its frequency, i.e., an n -photon subharmonic drive, which excites the qubit.

To investigate this process for fluxonium qubits, we bias the qubit at its lower sweet spot and apply a time-dependent drive to the flux line. The corresponding Hamiltonian in Eq. (3) can be separated into a time-independent

part \hat{H}_0 and a time-dependent drive term \hat{H}_d , given by

$$\hat{H}_0 = 4E_C \hat{n}^2 + E_J \cos \hat{\phi} + \frac{E_L}{2} \hat{\phi}^2, \quad (4)$$

$$\hat{H}_d(t) = -E_L \phi(t) \hat{\phi}, \quad (5)$$

where we have omitted global energy offsets (the sign change in Eq. (4) results from operating the qubit at its half-integer flux sweet spot, where $\cos(\hat{\phi} + \pi) = -\cos \hat{\phi}$). The time-dependent flux modulation has the form

$$\phi(t) = 2\pi \frac{\Phi}{\Phi_0} E(t) \cos(\omega_d t), \quad (6)$$

with drive frequency ω_d , pulse amplitude Φ , and a normalized pulse envelope $E(t)$. In experiment, we probe the excitation spectrum using pulsed qubit spectroscopy, by sweeping the drive frequency ω_d from $\omega_{\text{eg}}/8$ to $\omega_{\text{eg}}/3$ and measuring the excited-state population $P(|e\rangle)$, as shown in Fig. 2(a). This frequency range is selected to probe the most dominant multiphoton transitions by using a flat-top Gaussian pulse with drive amplitude $\Phi/\Phi_0 = 0.083$ and a pulse length of 850 ns. We observe multiple signal peaks at frequencies close to integer fractions of ω_{eg} . However, all transitions show a systematic shift to higher frequencies, making it challenging to unambiguously identify signal peaks with their respective photon number.

To quantitatively assess the drive-induced frequency shift, we repeat the spectroscopy with varying drive amplitude Φ around the frequency of the third subharmonic, as well as for a lower frequency range in which transitions with higher photon numbers are expected. The resulting spectroscopy for the third subharmonic, displayed in Fig. 2(c), shows that the frequency shift increases monotonically with Φ and converges to $\omega_{\text{eg}}/3$ at low drive powers. The low-frequency spectroscopy shown in Fig. 2(b) features similar transitions that increase monotonically with amplitude, as well as various transitions that exhibit a nontrivial dependence on the amplitude. We attribute these transitions to the drive-induced coupling of the qubit to other systems, such as the readout resonator, defects on the surface of the chip [48], or other parasitic resonances. A detailed study of the origin of the transitions is, however, beyond the scope of this work. We identify the spectral lines corresponding to a multiphoton drive by comparing the spectrum to numerical simulations of the time evolution of the ground state $|g\rangle$ under the Hamiltonian $\hat{H}_0 + \hat{H}_d(t)$ (see Appendix E). Remarkably, we find spectral lines for 9-, 11-, 13-, and 15-photon transitions (dashed red lines in Fig. 2), which highlights the strong nonlinearity of the fluxonium potential. All measured spectral resonances show a distinct shift in frequency compared to the power scaling predicted in simulations.

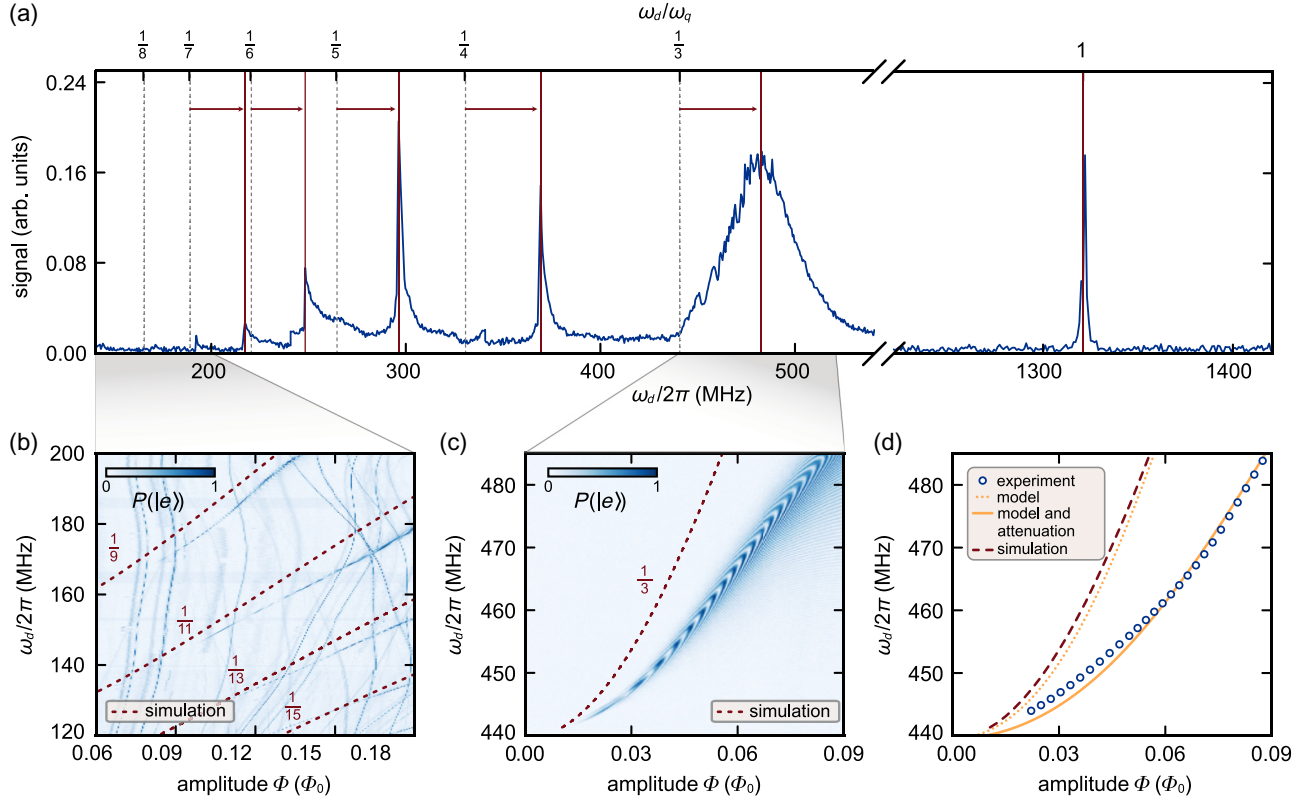


FIG. 2. Pulsed subharmonic qubit spectroscopy. (a) Qubit spectroscopy at a fixed amplitude. We observe qubit excitation at its transition frequency ω_{eg} and at fractions $1/n$ of ω_{eg} . The frequency range around ω_{eg} is measured by driving over the auxiliary MW line at -30 dB reduced power. (b),(c) The measured excited-state population of the qubit under subharmonic driving for varying drive amplitude and frequency ranges around $\omega_{eg}/3$ (c) and below $\omega_{eg}/9$ (b). The dashed lines indicate the simulated resonant drive frequency of the subharmonic transitions. (d) The resonant drive frequency of the third subharmonic as a function of the drive amplitude for data (blue circles), the model (dashed orange line), and simulations (dashed red line). Including a frequency-dependent attenuation of the flux-bias line results in good agreement between the model and the data (solid orange line).

In order to better understand the observed behavior, we derive an effective analytical model for the n -photon subharmonic drive. We start with Eq. (4) and express the undriven Hamiltonian \hat{H}_0 in terms of its eigenstates $|m\rangle$:

$$\hat{H}_0 = \hbar\omega_{eg}\hat{b}^\dagger\hat{b} + \frac{\hbar\alpha}{2}\hat{b}^\dagger\hat{b}^\dagger\hat{b}\hat{b} + \dots, \quad (7)$$

where we have introduced the ladder operator \hat{b} , defined as $\hat{b}|m\rangle = \sqrt{m}|m-1\rangle$, and the anharmonicity α of the qubit [49]. We emphasize that infinitely many terms in Eq. (7) are needed to adequately describe the fluxonium spectrum. Given that our fluxonium is less anharmonic than conventional implementations (cf. Appendix A), we neglect all but the first two terms, resulting in a three-level approximation, which is equivalent to numerical simulations that include the lowest 20 states and is sufficient to explain the observed 3-photon behavior quantitatively. Expressing the flux operator $\hat{\phi}$ in terms of \hat{b}^\dagger and \hat{b} , $\hat{H}_d(t)$ takes the form

$$\begin{aligned} \hat{H}_d &= -\phi(t)E_L\hat{\phi} \\ &= -\phi(t)[\beta_1(\hat{b} + \hat{b}^\dagger) + \beta_2(\hat{b}^\dagger\hat{b}\hat{b} + \hat{b}^\dagger\hat{b}^\dagger\hat{b})], \end{aligned} \quad (8)$$

with the coefficients $\beta_1 = E_L\langle g|\hat{\phi}|e\rangle$ and $\beta_2 = (E_L/\sqrt{2})\langle e|\hat{\phi}|f\rangle - \beta_1$, which determine the drive strength.

The emergence of n -photon transitions from $\hat{H}_0 + \hat{H}_d(t)$ is described perturbatively by a Magnus expansion [50] of the time evolution

$$\hat{U}(0, t_{\text{pulse}}) = \mathcal{T} \exp\left(-i \int_0^{t_{\text{pulse}}} dt \hat{H}(t)\right), \quad (9)$$

where \mathcal{T} denotes the time-ordering operator. Each expansion order is proportional to time integrals over the times t_i of the nested commutators $[\hat{H}(t_1), [\hat{H}(t_2), [\dots]]]$. A multiphoton drive arises only if $\hat{H}(t)$ contains terms where the nested commutator is proportional to \hat{b} or \hat{b}^\dagger and its oscillation period is on resonance with the shifted transition $\omega_{eg} + \delta$ of the driven fluxonium. When using bosonic operators, one can easily identify two operator pairs that satisfy these conditions for a drive frequency $\omega_d \sim \omega_{eg}/n$. The first noncommuting pair is the α term in \hat{H}_0 and the linear β_1 term in \hat{H}_d , i.e., when $n = 3$, $\beta_1^3[\hat{b}^\dagger, [\hat{b}^\dagger, [\hat{b}, (\alpha/2)\hat{b}^\dagger\hat{b}^\dagger\hat{b}\hat{b}]]] \propto \hat{b}^\dagger$. It can be understood as the drive term interacting with the anharmonicity of

the fluxonium. Furthermore, the second pair contains two drive terms proportional to β_1 and β_2 from \hat{H}_d , i.e., when $n = 3$, $\beta_1^2 \beta_2 [\hat{b}^\dagger, [\hat{b}, \hat{b}^\dagger \hat{b}^\dagger \hat{b}]] \propto \hat{b}^\dagger$. It can be interpreted as a self-interaction term of the drive operator. The resulting effective Hamiltonian for the n -photon drive, derived in detail in Appendix F, is given by

$$\frac{\hat{H}_{\text{eff},n}}{\hbar} = (\omega_{\text{eg}} + \delta_n - n\omega_d) \hat{b}^\dagger \hat{b} + \frac{\alpha + \alpha_n}{2} \hat{b}^\dagger \hat{b}^\dagger \hat{b} \hat{b} + \Omega_n (\hat{b}^\dagger + \hat{b}). \quad (10)$$

The drive induces a frequency shift on all energy eigenstates, here visible as δ_n and α_n for the first and second excited states $|m = 1\rangle$ and $|m = 2\rangle$, respectively. Additionally, $\hat{H}_{\text{eff},n}$ contains an effective coupling term Ω_n equal to the Rabi frequency when driven at the subharmonic frequency $\omega_d = (\omega_{\text{eg}} + \delta_n)/n$. The leading-order contribution to the frequency shift, denoted as $\delta_n^{(2)}$, arises from a second-order process related to self-interaction and its proportionality is given by

$$\delta_n^{(2)} \propto \frac{n}{(n-1)^2 \omega_d} \left[\langle g|\hat{\phi}|e\rangle^2 - \frac{1}{2} \langle e|\hat{\phi}|f\rangle^2 \right] \left(\frac{\Phi}{\Phi_0} \right)^2. \quad (11)$$

Thus, we can determine the sign of δ_n from the matrix elements of the drive operator $\hat{\phi}$ and for our device we expect positive frequency shifts. Note that for more anharmonic fluxonium qubits, δ_n increases strongly since ω_d decreases and the matrix-element asymmetry, here β_2 , increases. In comparison, the matrix asymmetry vanishes in transmon qubits, where $\langle e|\hat{\phi}|f\rangle = \sqrt{2} \langle g|\hat{\phi}|e\rangle$ or, equivalently, $\beta_2 = 0$; thus only higher order contributions determine the frequency shifts. In general, the Rabi frequency for an n -photon process Ω_n scales with the drive amplitude Φ according to a power law $\Omega_n \propto \Phi^n$, as derived in Appendix F. Similar to the expression for the frequency shift $\delta_n^{(2)}$, the dominant contribution to the scaling of Ω_n with respect to Φ in our system arises from a matrix-element asymmetry β_2 . This enables subharmonic transitions to appear at lower amplitudes compared to transmon qubits, which suggests that the fluxonium is a more suitable circuit for the application of subharmonic driving.

To confirm the predicted amplitude-dependent frequency shift as a function of the drive amplitude, we measure the qubit frequency at a fixed drive amplitude and optimize the drive parameters using an iterative tune-up procedure, as described in detail in Appendix G. The measured amplitude-dependent frequency shift [Fig. 2(d), blue circles], increases to first order quadratically as predicted. Its curvature is, however, smaller, which we attribute to the frequency-dependent transfer function of the flux line caused by the skin effect in the stainless-steel coaxial

wiring. The signal amplitude Φ_{qubit} arriving at the qubit can be approximately characterized by an attenuation factor a_0 quantifying the length, thickness, and conductivity of the inner conductor $\Phi_{\text{qubit}} = \Phi/(1 + a_0 \sqrt{\omega_d/2\pi})$ [51,52]. We achieve good agreement between the model and the data with an attenuation factor of $a_0 = 9.49(8) \times 10^{-5} \text{ Hz}^{-1/2}$, resulting from a least-squares fit with a_0 as the single free parameter. The model predicts a power loss of 6.0(1) dB at 1 GHz, consistent with the specified total power loss of approximately 5.7 dB at 1 GHz for the signal line used in the experiment, as described in Appendix B. It is important to note, however, that the actual transfer function may be more complex due to additional distortions caused by dielectric losses and impedance mismatches in the flux line [53].

IV. n -PHOTON RABI FREQUENCIES

Following the characterization of the frequency shift, we quantify the Rabi frequency Ω_n of the subharmonics $n = 3, 5, 7$, and 11 as a function of the drive amplitude Φ . For a fixed drive amplitude, varying the drive frequency and pulse length reveals characteristic chevron patterns for each subharmonic drive, as shown in exemplary form for

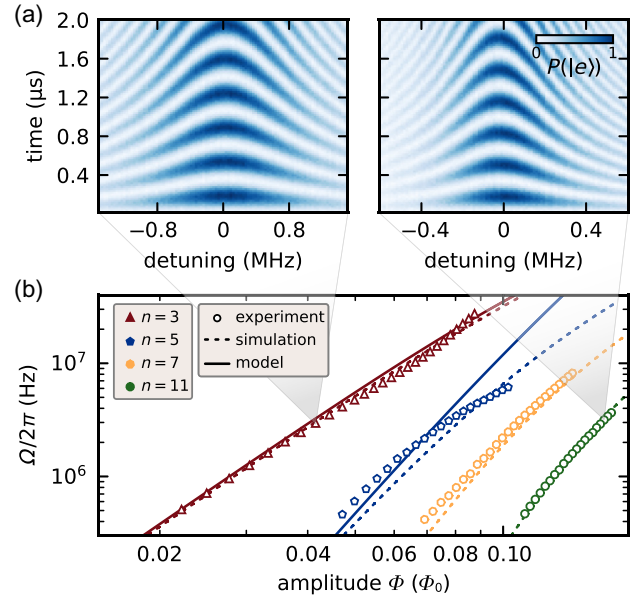


FIG. 3. Rabi frequencies for n -photon subharmonic drives. (a) The excited-state population as a function of the time and detuning for the third subharmonic at a drive amplitude of 41.5 mΦ₀ (left panel) and for the 11th subharmonic at a drive amplitude of 160.5 mΦ₀ (right panel). The detuning denotes the offset of the drive from the calibrated center frequency. The drive amplitudes are chosen to obtain similar Rabi frequencies of $\Omega/2\pi \sim 2.5$ MHz. (b) The Rabi frequencies Ω_n as a function of the pulse amplitude Φ for different subharmonic drives, compared to numerical simulation and the analytical model. The extracted error bars are smaller than the marker size.

the 3- and 11-photon transitions in Fig. 3(a). We extract Ω_n for each amplitude using an iterative gate tune-up routine as described in Appendix G. The resulting amplitude dependence of the Rabi frequency [Fig. 3(b)] agrees well with the analytical no-free-parameter model and numerical simulations for the third subharmonic when including the attenuation due to the skin effect discussed above. We use the same value of a_0 for all the subharmonic modes, which we have extracted from the frequency shift of the third subharmonic. The strong agreement between experiment, simulation, and theory highlights the validity of our model including the skin effect. Also for the fifth subharmonic, a comparison of the analytical solution and the experimental data shows good agreement at low drive powers, which demonstrates that the perturbative approach can be extended beyond the 3-photon processes. The three-level approximation of the fluxonium remains valid for describing higher photon processes. However, a clear discrepancy emerges between the experimental data and the model at higher amplitudes for the fifth subharmonic due to the limited order of the Magnus expansion. In contrast, the numerical simulation matches the experimental data qualitatively up to the 11th photon process. We attribute residual deviations between experiments and simulations to a nontrivial transfer function for the flux line caused by standing waves due to impedance mismatches (see Appendix H). After accounting for the influence of the skin effect, we fit the power scaling of each subharmonic with a leading-order exponent and find 2.81(1), 3.87(1), 4.73(1), and 5.78(1) for $n = 3, 5, 7$, and 11, respectively. This differs from the intuitive expectation that an n -photon process scales with Φ^n . In fact, the derivation in Appendix F demonstrates that a Φ^n scaling is only valid for small driving amplitudes. At higher drive amplitudes, correction terms such as Φ^{n+2} become significant, indicating the presence of additional coupling paths. The number of these paths can grow exponentially with increasing n [54], thereby modifying the simple power-law dependence of the Rabi rates and frequency shifts.

V. BENCHMARKING SINGLE-QUBIT GATES

To benchmark the performance of subharmonic driving for single-qubit gates, we compare three different configurations: a third subharmonic drive through the LP-filtered flux line (LP), a conventional resonant drive through the unfiltered flux line (UF) and a conventional resonant drive via the MW line. We use the third subharmonic as it shows a higher Rabi frequency for similar drive power compared to subharmonics with higher photon numbers, resulting in faster gate speeds at equal power levels (Fig. 3).

For gate calibration, we set a constant pulse amplitude of a pulse with a flat-top Gaussian envelope and optimize the frequency and time of the pulse. Additionally, we calibrate virtual-Z rotations to correct for phase

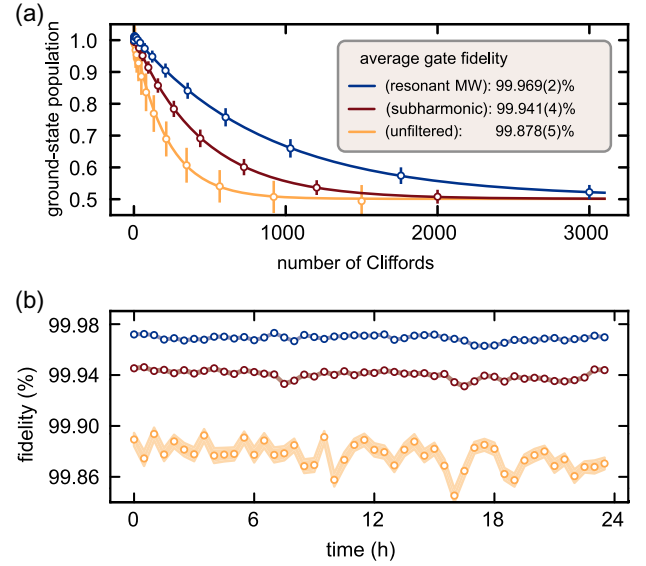


FIG. 4. The randomized benchmarking of resonant and subharmonic single-qubit gates. (a) The ground-state population as a function of the number of random Clifford gates averaged over 24 h. Each point is averaged over 1440 random sequences. (b) The time-resolved average gate fidelity measured over 24 h. Each data point shows the average gate fidelity obtained from 30 random sequences. The shaded region indicates one standard deviation.

changes acquired due to the power-dependent frequency shift during the pulse (Fig. 2). A detailed description of the tune-up procedure is provided in Appendix G. Similarly, we calibrate the on-resonance gate implemented using a derivative removal by adiabatic gate (DRAG) pulse [55]. All gates are set to an equal length of 64 ns to ensure that qubit coherence affects all gates similarly. We determine the gate fidelities of all three implementations through interleaved randomized benchmarking [Fig. 4(a)], where we use a gate set $\mathcal{G} = \{I, X_{\pm\pi}, Y_{\pm\pi}, X_{\pm\pi/2}, Y_{\pm\pi/2}\}$, resulting in an average of 1.875 gates per Clifford [56]. To test the stability of the subharmonic gate to setup-related drifts that might affect the Rabi frequency Ω_n and subsequently the frequency shift δ_n [33,57], we conduct repeated randomized-benchmarking experiments over a time period of 24 h. The averaged and time-resolved randomized-benchmarking experiments shown in Figs. 4(a) and 4(b) result in gate fidelities $\mathcal{F}_{\text{UF}} = 99.878(5)\%$ for the unfiltered flux-line configuration (UF) and in the LP-filtered configuration in $\mathcal{F}_{\text{SH}} = 99.941(4)\%$ for the subharmonic implementation, and $\mathcal{F}_{\text{MW}} = 99.969(2)\%$ for the MW-line implementation.

Using the measured T_1 and T_2^* times shown in Table I, we compare the obtained gate fidelities to the coherence limit [16,58]

$$\mathcal{F}^{\text{coh}} = 1 - \frac{t_g}{3} \left(\frac{1}{T_\phi} + \frac{1}{T_1} \right), \quad (12)$$

which results in coherence limits of $\mathcal{F}_{\text{UF}}^{\text{coh}} = 99.87(2)\%$ and $\mathcal{F}_{\text{LP}}^{\text{coh}} = 99.965(4)\%$ for the unfiltered and LP-filtered flux-line configuration, respectively, showing that both on-resonance gates are close to the coherence limit of the device. While the subharmonic gate shows a significantly improved fidelity compared to the unfiltered configuration, it does not reach the coherence limit. Numerical simulations of the subharmonic gate show an infidelity due to leakage into noncomputational states smaller than 10^{-5} (see Appendix E), suggesting that the observed infidelity is currently not limited by this effect. Instead, we identify three potential sources of infidelity arising from strong flux modulation, signal-line distortions of the pulse, and the dynamic frequency shift during the gate. First, strong low-frequency flux modulations have been demonstrated in theory [59] and experiment [60] to affect qubit coherence by creating Floquet quasienergy eigenstates, where the contribution of noise is averaged out over one modulation period. As strong modulations enhance coherence only within a narrow range of drive amplitudes and frequencies, we consider it likely that the strong pulsed drive applied in our experiment leads to a reduction in qubit coherence not benefiting from the noise cancellation effect, thus negatively impacting gate performance. Second, signal-line distortion is a common problem detected in experiments [53]. In our experimental setup, we observe a signal echo 10 ns after the pulse, reducing the fidelity of consecutive gates. To reduce this effect, we include a 24-ns and 32-ns delay subsequent to the π and $\pi/2$ pulses within the 64-ns gate duration. To address this source of infidelity more directly, one can predistort the input pulse shape to account for the transfer function of the flux line after characterizing the step response with a cryoscope experiment [53]. Third, the gate fidelity could potentially be improved by accounting for the dynamic frequency shift during the gate operation. During the rise time of the flat-top Gaussian pulse, the qubit frequency shifts gradually, causing the drive frequency ω_d to become resonant with the subharmonic transition only after the rise is complete. By tracking this frequency shift, the drive could remain on resonance throughout the entire gate duration, thereby improving both the gate speed and the fidelity.

We assess the stability of the different gate implementations by the variance of the gate fidelity shown in Fig. 4(b), where the average gate fidelity is obtained from 30 random Clifford sequences for 24 h, with a cadence of 30 min. Using the variance of the MW gate as a reference, we calculate the relative variance of the other gates to be $\sigma_{\text{SH}}^2/\sigma_{\text{MW}}^2 = 2.3$ for the subharmonic gate and $\sigma_{\text{UF}}^2/\sigma_{\text{MW}}^2 = 19.9$, showing that the subharmonic gate exhibits almost equal stability compared to the on-resonance MW gate and a close to one-order-of-magnitude improvement to the resonant flux-line implementation without a filter, which is more sensitive to temperature fluctuations due to the $T_1 \propto 1/(2n_{\text{th}} + 1)$ dependence [43].

VI. CONCLUSIONS AND OUTLOOK

In conclusion, we have demonstrated that a single low-pass-filtered flux-control line is sufficient to realize universal high-fidelity control of a fluxonium qubit via subharmonically driven multiphoton transitions, while simultaneously suppressing relaxation and dephasing due to control-line noise. We have developed a theoretical model for subharmonic driving in strongly anharmonic systems that accurately predicts drive-induced frequency shifts and Rabi frequencies. The model reveals enhancement of the subharmonic Rabi frequency arising from matrix-element asymmetries, emphasizing that subharmonic control is intrinsically more effective in fluxonium qubits than in weakly anharmonic systems such as transmons. Experimentally, we have demonstrated qubit control ranging from 3- to 11-photon processes, confirming that subharmonic control is particularly effective in fluxonium qubits. The use of optimized flat-top Gaussian pulses leads to gate fidelities exceeding 99.94%, approaching the fidelities achieved via conventional on-resonant driving, which are close to the coherence limit of the device. By further optimization using closed-loop schemes [61,62] and predistorted pulses to correct for signal distortions in the coaxial cable [53], we expect that the performance of subharmonic gates will equal that of on-resonance gates in the near future.

The on-chip integration of reflective low-pass filters will mitigate the remaining decay attributed to losses in the flux-line segment that connects the chip to the filter. Moreover, the strong amplitude dependence of multiphoton transitions offers increased flexibility in choosing the drive frequency, which can be used to mitigate crosstalk [63]. Off-resonant driving of neighboring qubits is further reduced due to the higher-order amplitude dependence of the Rabi frequency compared to on-resonance driving.

By combining dc flux biasing and high-fidelity transversal control into a single Purcell-protected channel, our approach establishes a scalable and hardware-efficient control architecture for fluxonium-based processors, matching fixed-frequency transmons in terms of wiring simplicity. Beyond fluxonium qubits, subharmonic control exploits the presence of higher-lying energy levels to enable transitions that are otherwise forbidden by selection rules or suppressed by frequency filtering, provided that appropriate matrix elements exist. This makes it a promising strategy for controlling other strongly anharmonic qubit circuits, such as qudits and protected qubits, where transitions between computational states are exponentially suppressed but transitions to higher levels remain accessible.

ACKNOWLEDGMENTS

We thank Jacquelin Luneau and Peter Rabl for insightful discussions and helpful comments. This work received financial support from the German Federal Ministry of

Education and Research via the funding program “Quantum Technologies—from Basic Research to the Market” under Grant No. 13N15680 (German Quantum Computer based on Superconducting Qubits, GeQCoS) and under Grant No. 13N16188 (Munich Quantum Valley Quantum—Computer Demonstrators, MUNIQC-SC), by the Deutsche Forschungsgemeinschaft (DFG, German Research Foundation) via Grant No. FI2549/1-1, and via Germany’s Excellence Strategy EXC-2111-390814868 “MCQST,” as well as by the European Union (EU) through the EU Flagship on Quantum Technology HORIZON-CL4-2022-QUANTUM-01-SGA Grant No. 101113946 (OpenSuperQPlus100). The research is part of the Munich Quantum Valley, which is supported by the Bavarian State Government with funds from the Hightech Agenda Bayern Plus.

DATA AVAILABILITY

The data that support the findings of this paper are openly available [64].

APPENDIX A: DEVICE PARAMETERS

In Fig. 5(a), we show a lumped-element circuit of the qubit used in this work, including characterization measurements for the device in Figs. 5(b) and 5(c). We realize the qubit with a niobium ground plane on a high-resistivity silicon substrate and with Al/AIO_x/Al Josephson junctions for both the phase-slip junction and the inductance. The inductance is split into two arrays, allowing for galvanic connection of the flux line [18,65]. The coupling of the flux line to the qubit is given by their shared inductance M . Both the readout resonator as well as the MW drive line are coupled capacitively, predominantly to one of the two qubit islands. From qubit spectroscopy of the fundamental mode, depicted in Fig. 5(b), and comparing to eigenenergy simulations of the equivalent circuit obtained using the ScQubits software package [66,67], we determine the circuit parameters $E_J/h = 1.69$ GHz, $E_L/h = 1.07$ GHz and $E_C/h = 0.68$ GHz, resulting in a qubit frequency $\omega_{eg}/2\pi = 1.32$ GHz and an anharmonicity $\alpha/2\pi = 0.81$ GHz. The mutual inductance value $M = 3.4$ pH is determined following a calculation given in Appendix D. In Fig. 5(c), we show exemplary single-trace measurements for the energy relaxation time T_1 (left) and the Ramsey-coherence time T_2^* of the device. For a more detailed analysis, see Sec. II.

APPENDIX B: EXPERIMENTAL SETUP

The sample is mounted at the mixing-chamber stage of a dilution refrigerator (Bluefors XLD1000sl). In Fig. 6, we display the full electronic setup up to the room-temperature control. We employ two devices for qubit control. A Zurich

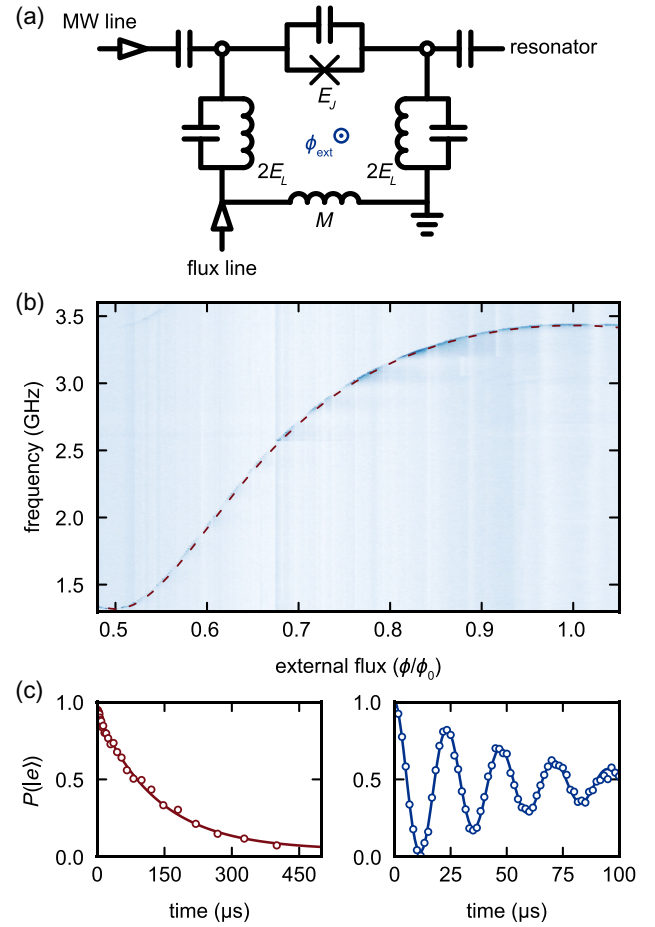


FIG. 5. Device characterization. (a) The equivalent circuit of the fluxonium qubit, realized with a Josephson junction with energy E_J , a split inductance with inductive energy E_L , and a total capacitive energy E_C . (b) Pulsed spectroscopy of the fundamental fluxonium mode as a function of the external flux. The red line represents the transition frequency obtained from circuit simulations. (c) Exemplary decay (left panel) and coherence (right panel) measurements of the device using subharmonic driving.

Instruments quantum controller (SHFQC) is used for driving the qubit at microwave frequencies and for readout of the qubit state, while a single channel of a Zurich Instruments arbitrary waveform generator (HDAWG) is utilized for dc-flux biasing and ac-flux control. 50 dB of attenuation combined with a 2-GHz low-pass filter (KL 6L250-2000) ensure a low-noise MW control line. The SHFQC generates and digitizes the readout signal. With a HEMT (LNF-LNC4_8C) and a room-temperature amplifier (Qotana DBLNA104000800F), we achieve a state-assignment fidelity of $F_{\text{readout}} \approx 94\%$. We use a high-pass filter (Minicircuits VHF-5050+) at the input and output ports of the readout line, in combination with two dual-junction isolators (LNF-ISISC4_12A) at the output to protect the qubits from unwanted noise photons in resonators. Flux control is achieved with a single line that is attenuated by 20 dB at the 3-K stage. Through a switch

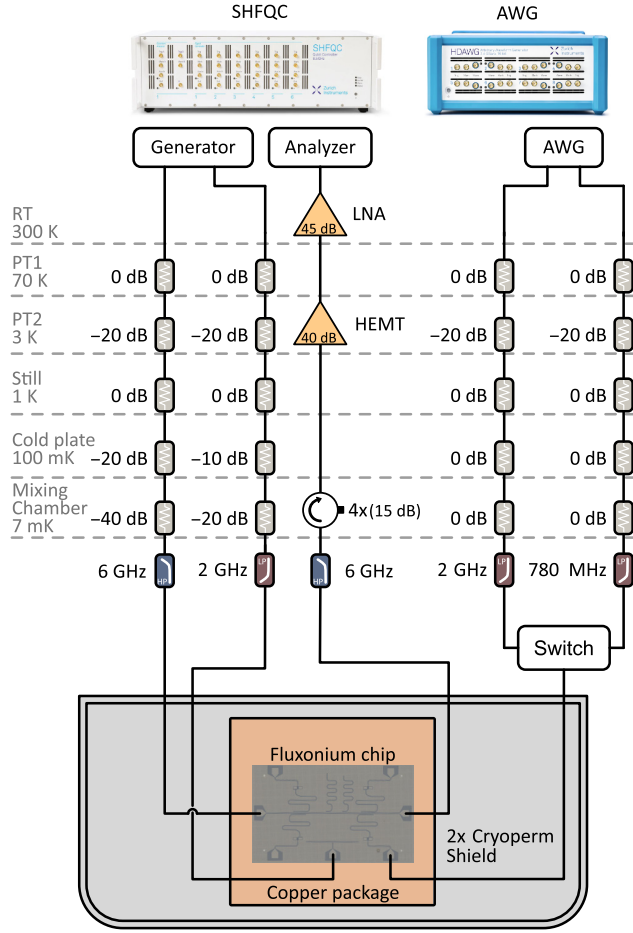


FIG. 6. The experimental setup. The qubit chip is mounted inside two Cryoperm shields to protect it from stray magnetic fields (for details, see the main text).

(Radiall R573423600), we test different filter configurations at the 7-mK plate. The chip is packaged and mounted inside two Cryoperm shields. To estimate the losses of the flux line, we characterize the 3-m room-temperature coaxial cable using a vector network analyzer (VNA), resulting in 2.5 dB of attenuation at 1 GHz. Inside the cryostat, we assume a total length of 1.05 m, with attenuation of around 3 dB at 1 GHz, extracted from the Bluefors specification sheet [23]. This results in a total power loss of around -5.7 dB at 1 GHz, which agrees well with the value of $-6.0(1)$ dB predicted from the skin effect described in Sec. III.

APPENDIX C: T_2 -LIMIT

There are two main sources of noise that lead to dephasing and subsequently to a reduction of the coherence time [68]. On the one hand, low-frequency noise that exhibits the characteristic $1/f$ behavior in the power spectral density over the frequency is present in the system [44]. On the other hand, fluctuations of the photon number in the readout resonator dispersively shift the frequency of the

qubit and lead to dephasing of the qubit. We can express the effect of thermal-resonator photons $n_{\text{th}} < 1$ on the qubit dephasing time T_ϕ as [69]

$$\frac{1}{T_\phi} = \frac{\kappa (2\chi)^2}{\kappa^2 + (2\chi)^2} n_{\text{th}}. \quad (\text{C1})$$

Here, κ is the resonator linewidth, χ is the dispersive shift, and n_{th} is the average thermal-resonator population. The dephasing rate decreases the maximum coherence time as

$$\frac{1}{T_2} = \frac{1}{2T_1} + \frac{1}{T_\phi}. \quad (\text{C2})$$

By measuring T_1 and T_2 , and assuming that the fluxonium is first-order protected from flux noise at its sweet spot, we extract the resonator population and calculate an effective resonator temperature using Eq. (C1) and Eq. (C2). For our experimental parameters $\kappa/2\pi = 1.2$ MHz, $2\chi/2\pi = 5.3$ MHz, $\omega_R/2\pi = 6.9$ GHz, $T_2 = 75(9)$ μs and $T_1 = 168(20)$ μs (see Table I), resulting in an effective resonator temperature of 51(1) mK.

APPENDIX D: QUBIT TEMPERATURE AND BATH COUPLING

We extract the effective qubit temperature from single-shot measurements of the thermal population of the qubit, shown in Fig. 7. The qubit temperature is approximated by [70]

$$T_{\text{eff}} = -\frac{\hbar\omega}{k_B} \ln \left(\frac{P(|e\rangle)}{P(|g\rangle)} \right)^{-1}, \quad (\text{D1})$$

where \hbar is the reduced Planck's constant, k_B is the Boltzmann constant, and $P(|e\rangle)$ ($P(|g\rangle)$) is the probability of finding the qubit in the ground state $|g\rangle$ (excited state $|e\rangle$), respectively. In Fig. 7, we show the measured ground-state population $P(|g\rangle)$ for the filtered [Fig. 7(a)] and unfiltered [Fig. 7(b)] configurations. By fitting the data with a double Gaussian and extracting the relative magnitude of the

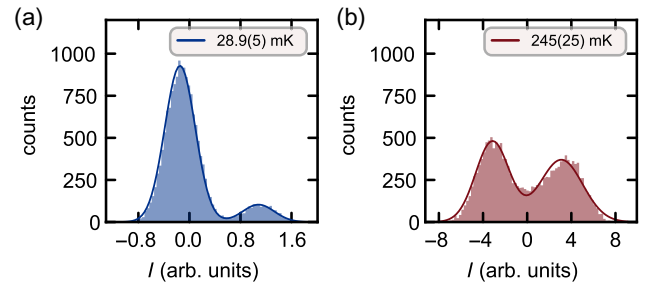


FIG. 7. Thermal-state measurements of different filter configurations. The thermal state projected onto the state discrimination axis: (a) filtered configuration; (b) unfiltered configuration.

peak heights, we extract effective qubit temperatures of $T = 28.9(5)$ mK and $T = 245(25)$ mK for the filtered and unfiltered case, respectively. In the following, we provide an estimate for the qubit-bath coupling via the flux line. The average thermal-bath photon number at a frequency ν and temperature T is given by the Bose-Einstein statistic:

$$n_{\text{th}} = \left[\exp\left(\frac{\hbar\omega}{k_B T}\right) - 1 \right]^{-1}. \quad (\text{D2})$$

We calculate the decay rate caused by baths i coupled to the qubit with a coupling rate γ_i by [43]

$$\gamma(T) = \sum_i \gamma_i [2n_{\text{th},i}(T) + 1]. \quad (\text{D3})$$

By adding a filter on the line, we reduce the coupling rate to the bath by the attenuation of that filter. Thus we can extract the initial bath coupling rate γ_0 by taking the difference of the decay rates between the filtered (f) and unfiltered (uf) cases:

$$(1/T_{1,\text{LP}} - 1/T_{1,\text{UF}}) = \gamma_0(A - 1)(2n_{\text{th}} + 1), \quad (\text{D4})$$

where A is the power attenuation factor of the filter at the qubit frequency and $\gamma = 1/T_1$. Using experimental values stated in Sec. II, an attenuation factor $A = 10^{-3.55}$ of the filter at the qubit frequency, and a bath temperature of 3 K, we estimate a decay time into this channel of $1/\gamma_0 = 3.6(5)$ ms. From this result, we can extract the mutual inductance M between the qubit and the flux line. The equation relating γ_{eg} and M can be derived from Fermi's golden rule, following [4,36]

$$\gamma_{\text{eg}} = \frac{\omega_{\text{eg}} R_Q R M^2}{2\pi |Z|^2 L^2} |\langle g|\hat{\phi}|e\rangle|^2 \left[1 + \coth\left(\frac{\hbar\omega_{\text{eg}}}{2k_B T}\right) \right], \quad (\text{D5})$$

where Z is the impedance of the flux line, L is the inductance of the qubit, and $R_Q = h/(2e)^2$ is the superconducting resistance quantum. Using the qubit parameters from Appendix A and solving Eq. (D5) for M , we obtain $M_{\text{Exp}} = 3.1(2)$ pH in the limit of $T = 0$, which is close to the design value of 3.2 pH simulated using the 3D-MLSI software package [71]. Equivalently, using M_{Design} in Eq. (D5) gives $\gamma_0 = 1/3.4$ ms. We simulate the relevant matrix elements for our circuit using the ScQubits software package [66,67].

APPENDIX E: NUMERICAL SIMULATIONS

To extract the position of subharmonic drive frequencies ω_d and their respective Rabi frequencies Ω at different drive amplitudes Φ , we use a discretized approach for the simulation of the time dynamics of our system. We start

with the Hamiltonian with an applied static flux bias of $0.5 \Phi_0$:

$$\hat{H}(t) = 4E_C \hat{n}^2 + E_J \cos \hat{\phi} + \frac{E_L}{2} [\hat{\phi} - \phi(t)]^2. \quad (\text{E1})$$

We then diagonalize numerically for zero applied flux, yielding the eigenstates $|\psi_i\rangle$, which we truncate to the 20 lowest-energy eigenstates to reduce computation time, while maintaining very good numerical precision. We then discretize the pulse shape

$$\phi(t_j) = 2\pi \frac{\Phi}{\Phi_0} E(t_j) \cos(\omega_d t_j), \quad (\text{E2})$$

where $E(t)$ is the pulse envelope and ω_d is the drive frequency. We use a time resolution of $t_{j+1} - t_j = 0.1$ ns such that the oscillation frequency of the drive is slow compared to the time interval. The time evolution of the system is simulated by iteratively applying the time-evolution operator. For each time slice t_j , the state after discretized time evolution is given by

$$|\psi(t_{j+1})\rangle = \exp\left(-i \frac{\hat{H}(t_{j+1})t_j}{\hbar}\right) |\psi(t_j)\rangle, \quad (\text{E3})$$

with the initial condition $|\psi(0)\rangle = |g\rangle$. After completion of the time evolution at the pulse length t_{pulse} , we extract the excited-state population from the overlap $\langle e|\psi(t_{\text{pulse}})\rangle$. We find the transitions corresponding to subharmonic processes with an iterative optimization. For a fixed drive amplitude, we perform an interleaved optimization of the drive frequency and pulse time for applying an on-resonance π rotation, optimizing one parameter while keeping the other fixed.

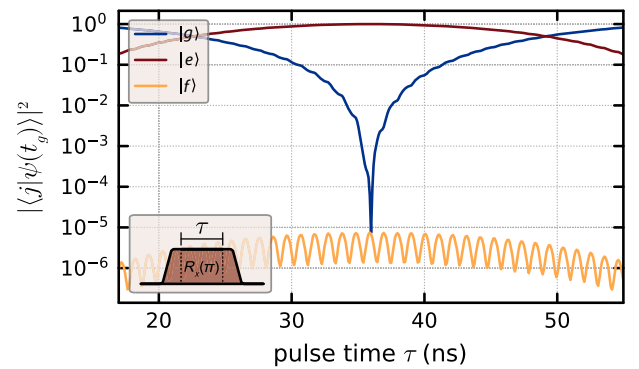


FIG. 8. The simulated state overlap versus the pulse duration. We simulate the time evolution of the fluxonium qubit driven at $\omega_d = 480$ MHz with a drive amplitude of $\Phi = 5.25 \text{ m}\Phi_0$, while varying the duration τ of the flat section of a flat-top Gaussian pulse. The state populations of the computational states $|g\rangle$, $|e\rangle$, and $|f\rangle$ are shown as a function of τ . The inset illustrates the relation between τ and the overall pulse shape. The total rise and fall times of the pulse sum to 16 ns.

To assess the coherent error of the subharmonic single-qubit gate shown in Sec. V, we simulate the time evolution at $\omega_d = 480$ MHz, corresponding to a drive amplitude $\Phi = 5.25 m\Phi_0$ for different pulse lengths, as shown in Fig. 8. At the optimal pulse time for a π pulse, the fidelity is limited by leakage into the $|f\rangle$ state to 7.4×10^{-6} , which is well below the experimentally observed gate fidelity.

APPENDIX F: MODEL

In this appendix, we derive an analytical model describing the subharmonic driving of a fluxonium qubit at its third subharmonic. Higher-order harmonics can be performed analogously. The analytical expressions for fifth subharmonics are used in Fig. 3, even though not explicitly stated here.

A flux-driven fluxonium, biased at flux sweet spot $0.5\Phi_0$, is described by the following Hamiltonian ($\hbar = 1$) [60]:

$$\hat{H}(t) = 4E_C \hat{n}^2 + E_J \cos \hat{\varphi} + \frac{E_L}{2} [\hat{\varphi} - \phi(t)]^2, \quad (\text{F1})$$

with parameter definitions the same as those for Eq. (3). By expanding the square, we can remove a time-dependent global energy shift from the system and find that the resulting drive part of the Hamiltonian is actually linear in $\phi(t)$.

By diagonalizing the rest-frame Hamiltonian $\hat{H}_0 = \hat{H}|_{\phi=0}$ and utilizing the ladder operators, \hat{b} and \hat{b}^\dagger , in the energy basis of the fluxonium, i.e., $\hat{b}|n\rangle = \sqrt{n}|n-1\rangle$, the system takes the form

$$\hat{H}(t) = \hat{H}_0 - \phi(t) E_L \hat{\varphi}, \quad (\text{F2})$$

$$\hat{H}_0 = \omega_{\text{eg}} \hat{b}^\dagger \hat{b} + \frac{\alpha}{2} \hat{b}^\dagger \hat{b}^\dagger \hat{b} \hat{b} + \dots, \quad (\text{F3})$$

where the qubit frequency is ω_{eg} and α is its anharmonicity. The terms proportional to higher powers of \hat{b} are suppressed for the moment and are subrelevant for the Rabi oscillation.

The next step is to express the drive term linear in $\hat{\varphi}$ in the same basis. For that, we realize that \hat{H}_0 in its formulation, given in Eq. (F1), is symmetric in φ ; hence its eigenfunctions $|m\rangle$ need to be either symmetric or asymmetric in φ . Therefore, the matrix elements $\langle m|\hat{\varphi}|m'\rangle$ can only be nonvanishing if $m - m'$ is odd. Given that in our application the matrix elements are sufficiently small for $m - m' \leq 3$, the driven part of the Hamiltonian can be fully characterized by $\sum_n \beta_n \langle m - 1|\hat{\varphi}|m\rangle/\sqrt{m}$. Without loss of generality, we can therefore express

$$E_L \hat{\varphi} = \beta_1 (\hat{b} + \hat{b}^\dagger) + \beta_2 (\hat{b}^\dagger \hat{b} \hat{b} + \hat{b}^\dagger \hat{b}^\dagger \hat{b}) + \dots \quad (\text{F4})$$

We note again that terms with powers of \hat{b} higher than 3 exist but are not relevant to accurately describe Rabi oscillations.

We are interested in the effective dynamics of the model, given by

$$\hat{U}(0, t_{\text{pulse}}) = \mathcal{T} \exp \left(-i \int_0^{t_{\text{pulse}}} dt \hat{H}(t) \right), \quad (\text{F5})$$

denoting the time-ordered exponential. To study the n^{th} subharmonic drive, it is useful to go into a frame that rotates at n times the driving frequency, ω_d . The frame change is achieved by the unitary transformation $\hat{R}(t) = \exp(itn\omega_d \hat{b}^\dagger \hat{b})$. Further, to work with unitless quantities, we rescale the rotating system by $t \mapsto \tau = 2t\omega_d$ and $\hat{H}(t) \mapsto \hat{\tilde{H}}(\tau) := (\hat{R}\hat{H}(t)\hat{R}^\dagger - \hat{R}\hat{R}^\dagger)/(2\omega_d)$. Here, we are focusing on the third subharmonic and thus express the Hamiltonian in a rescaled 3-photon frame as

$$\hat{\tilde{H}}(\tau) = \frac{\Delta}{2\omega_d} \hat{b}^\dagger \hat{b} + \frac{\alpha}{4\omega_d} \hat{b}^\dagger \hat{b}^\dagger \hat{b} \hat{b} - \frac{\bar{\phi}}{2\omega_d} E(t) \left((e^{i\tau} + e^{i2\tau})(\beta_1 \hat{b} + \beta_2 \hat{b}^\dagger \hat{b} \hat{b}) + h.c. \right) + \dots, \quad (\text{F6})$$

where we denote the detuning between the qubit frequency and the triple-drive frequency by $\Delta = \omega_{\text{eg}} - 3\omega_d$ and use $\phi(t) = \bar{\phi} E(t) \cos(\omega_d t)$, where $E(t)$ is an envelope function with unit amplitude.

Working in the dispersive regime, we assume the following quantities to be small:

$$\Delta/(2\omega_d) \ll 1, \quad \alpha/(4\omega_d) \ll 1, \quad \beta_m \bar{\phi}/(2\omega_d) \ll 1. \quad (\text{F7})$$

In the regime in which Eq. (F7) holds, one expects that the time evolution can be well approximated by a power series

with respect to those small quantities, with a convergence rate given by Eq. (F7). Hence, we denote $\hat{\tilde{H}} \equiv \mathcal{O}(\omega_d^{-1})$. We want to stress at this point that the device is not in the low-frequency fluxonium regime and $\alpha/(4\omega_d) \sim 0.5$. For heavy fluxonia $\alpha \gg \omega_d$, the approximation by a power series in Eq. (F7) no longer holds. It is possible to reformulate the equations to account for general α/ω_d ; however, this requires a more careful investigation, which is beyond the scope of this paper [54].

A well-known procedure to perturbatively obtain the finite-time evolution operator from a time-dependent

Hamiltonian is the Magnus expansion [50]. Further, for a periodically driven system, the extended Floquet-Magnus expansions can be used to obtain an effective Hamiltonian, which is already implemented in time-modulated cold-atom systems [72]. The aim of Floquet-Magnus expansions is to move into a frame in which the Hamiltonian becomes independent of the fast-rotating contributions, i.e., we aim for a unitary transformation $\hat{U}(\tau) = \exp(i\hat{K}(\tau))$ such that

$$\hat{H}_{\text{eff}} = \hat{U}\hat{H}\hat{U}^\dagger - i\hat{U}\partial_\tau\hat{U}^\dagger \quad (\text{F8})$$

becomes independent of terms of the form $\exp(ik\tau)$. Note that the time dependence of the envelope function $E(t)$ remains, which can be assumed to be slow since the time length of $\dot{E}(t)$ is negligible compared to the pulse time. To eliminate rapidly oscillating terms, we generate $\hat{K}(\tau)$ iteratively by powers of Eq. (F7), i.e., we define

$$\begin{aligned} \hat{H} &= \sum_k e^{ik\tau} \hat{H}_k, \quad \hat{H}_k \equiv \mathcal{O}(\omega_d^{-1}), \\ \hat{H}_{\text{eff}} &= \sum_n \hat{H}_{\text{eff}}^{(n)}, \quad \hat{H}_{\text{eff}}^{(n)} \equiv \mathcal{O}(\omega_d^{-n}), \\ \hat{K}(\tau) &= \sum_n \hat{K}^{(n)}, \quad \hat{K}^{(n)} = \sum_{k \neq 0} e^{ik\tau} \hat{K}_k^{(n)}, \\ \hat{H}_k^{(n)} &\equiv \mathcal{O}(\omega_d^{-n}). \end{aligned} \quad (\text{F9})$$

Expanding Eq. (F8) in powers of $1/\omega_d$, we obtain the defining equation for $\hat{H}_{\text{eff}}^{(n)}$ and $\hat{K}_k^{(n)}$. At first order, it reads

$$\hat{H}_{\text{eff}}^{(1)} = \hat{H}(\tau) - \partial_\tau \hat{K}^{(1)} \quad (\text{F10})$$

and by defining $\hat{K}^{(n)}$ such that it collects all τ dependency inside it, the Hamiltonian becomes effectively time independent,

$$\hat{H}_{\text{eff}}^{(1)} = \hat{H}_0, \quad \hat{K}_k^{(1)} = \frac{\hat{H}_k}{ik}. \quad (\text{F11})$$

One proceeds similarly for higher orders:

$$\begin{aligned} \hat{H}_{\text{eff}}^{(2)} &= [i\hat{K}^{(1)}, \hat{H}] - \frac{1}{2}[i\hat{K}^{(1)}, \partial_\tau \hat{K}^{(1)}] - \partial_\tau \hat{K}^{(2)} \\ \Leftrightarrow \hat{H}_{\text{eff}}^{(2)} &= \sum_{k \neq 0} \frac{[\hat{H}_k, \hat{H}_{-k}]}{2k}, \\ \hat{K}_k^{(2)} &= \frac{[\hat{H}_k, \hat{H}_0]}{ik^2} + \sum_{k' \neq 0} \frac{[\hat{H}_{k'}, \hat{H}_{k-k'}]}{2ik'k}, \end{aligned} \quad (\text{F12})$$

$$\begin{aligned} \hat{H}_{\text{eff}}^{(3)} &= [i\hat{K}^{(2)}(\tau), \hat{H}(\tau)] + \frac{1}{2}[i\hat{K}^{(1)}(\tau), [i\hat{K}^{(1)}(\tau), \hat{H}(\tau)]] \\ &\quad - \frac{1}{2}[i\hat{K}^{(2)}(\tau), \partial_\tau \hat{K}^{(1)}(\tau)] - \frac{1}{2}[i\hat{K}^{(1)}(\tau), \partial_\tau \hat{K}^{(2)}(\tau)] \\ &\quad - \frac{1}{6}[i\hat{K}^{(1)}(\tau), [i\hat{K}^{(1)}(\tau), \partial_\tau \hat{K}^{(1)}(\tau)]] - \partial_\tau \hat{K}^{(3)}(\tau) \\ \Leftrightarrow \hat{H}_{\text{eff}}^{(3)} &= \sum_{k \neq 0} \frac{[[\hat{H}_k, \hat{H}_0], \hat{H}_{-k}]}{2k^2} \\ &\quad + \sum_{\substack{k, k' \neq 0 \\ k-k' \neq 0}} \frac{[[\hat{H}_{k'}, \hat{H}_{k-k'}], \hat{H}_{-k}]}{4k} \left(\frac{1}{k'} + \frac{1}{3(k' - k)} \right) \\ \dots \end{aligned} \quad (\text{F13})$$

Note, that we omit the definition of $\hat{K}^{(3)}$ as it is not relevant in order to obtain the effective Hamiltonian at third order.

It can be shown that $\hat{K}^{(n)}$ always depends on the envelope function, such that $\exp(i\hat{K}(\tau=0)) = \exp(i\hat{K}(\tau=2\omega_d t_{\text{pulse}})) = \mathbb{1}$ for an envelope function that vanishes at the beginning and the end of the pulse, e.g., a flat-top Gaussian. Therefore, the effective Hamiltonian captures the dynamics of the full gate.

Explicitly for the 3-photon process described by \tilde{H} in Eq. (F6), we obtain the effective Hamiltonian

$$\hat{H}_{\text{eff},3}^{(1)} = \Delta \hat{b}^\dagger \hat{b} + \frac{\alpha}{2} \hat{b}^\dagger \hat{b}^\dagger \hat{b} \hat{b}, \quad (\text{F14})$$

$$\hat{H}_{\text{eff},3}^{(2)} = -\frac{3\beta_2(2\beta_1 + \beta_2)}{8\omega_d} E^2 \bar{\phi}^2 \hat{b}^\dagger \hat{b}, \quad (\text{F15})$$

$$\hat{H}_{\text{eff},3}^{(3)} = \frac{5(\alpha(\beta_1 + \beta_2)^2 + \beta_2(2\beta_1 + \beta_2)\Delta)}{32\omega_d^2} E^2 \bar{\phi}^2 \hat{b}^\dagger \hat{b} + \frac{\beta_1\beta_2(2\beta_1 + \beta_2)}{32\omega_d^2} E^3 \bar{\phi}^3 (\hat{b}^\dagger + \hat{b}), \quad (\text{F16})$$

$$\begin{aligned} \hat{H}_{\text{eff},3}^{(4)} &= -\frac{21\beta_2^2(7\beta_1^2 + 10\beta_1\beta_2 + 4\beta_2^2)}{512\omega_d^3} E^4 \bar{\phi}^4 \hat{b}^\dagger \hat{b} - \frac{9(\alpha(\beta_1 + \beta_2)^2(\alpha + 2\Delta) + \beta_2(2\beta_1 + \beta_2)\Delta^2)}{128\omega_d^3} E^2 \bar{\phi}^2 \hat{b}^\dagger \hat{b} \\ &\quad + \frac{\beta_1(6\alpha(\beta_1 + \beta_2)^2 + 13\beta_2(2\beta_1 + \beta_2)\Delta)}{768\omega_d^3} E^3 \bar{\phi}^3 (\hat{b}^\dagger + \hat{b}), \end{aligned} \quad (\text{F17})$$

$$\begin{aligned}
\hat{H}_{\text{eff},3}^{(5)} = & \frac{\alpha\beta_2(313\beta_1 + 527\beta_2)(\beta_1 + \beta_2)^2}{2048\omega_d^4} E^4 \bar{\phi}^4 \hat{b}^\dagger \hat{b} + \frac{107\beta_2^2(7\beta_1^2 + 10\beta_1\beta_2 + 4\beta_2^2)\Delta}{2048\omega_d^4} E^4 \bar{\phi}^4 \hat{b}^\dagger \hat{b} \\
& + \frac{17(\alpha(\beta_1 + \beta_2)^2(\alpha^2 + 3\alpha\Delta + 3\Delta^2) + \beta_2(2\beta_1 + \beta_2)\Delta^3)}{512\omega_d^4} E^2 \bar{\phi}^2 \hat{b}^\dagger \hat{b} \\
& + \left(\frac{\beta_1(29\beta_2(2\beta_1 + \beta_2)\Delta^2 + 6\alpha(\beta_1 + \beta_2)^2(\alpha + 3\Delta))}{3072\omega_d^4} E^3 \bar{\phi}^3 + \frac{\beta_1\beta_2^2(29\beta_1^2 + 38\beta_1\beta_2 + 14\beta_2^2)}{1024\omega_d^4} E^5 \bar{\phi}^5 \right) (\hat{b}^\dagger + \hat{b}).
\end{aligned} \tag{F18}$$

Computing the effective Hamiltonian up to the fifth order provides a good match with the experimental data of the device. If one were to delve deeper into the fluxonium regime, i.e., increasing the ratios in Eq. (F7) of the relevant quantities versus ω_{eg} , higher orders of the power series would be necessary. On the other hand, high-frequency devices (such as transmon qubits) are found to have very low ratios and will, in general, require much lower orders

to be captured accurately (e.g., enabling tools such as the rotating-wave approximation).

Next to $\Delta \hat{b}^\dagger \hat{b}$ in Eq. (F14), we see that the higher orders of the effective Hamiltonian also contain diagonal terms. The collection of those additional terms proportional to $\hat{b}^\dagger \hat{b}$ in Eqs. (F15)–(F18) is called the subharmonic drive-induced Stark shift:

$$\begin{aligned}
\delta_3 = & -\frac{3\beta_2(2\beta_1 + \beta_2)}{8\omega_d} E^2 \bar{\phi}^2 + \frac{5(\alpha(\beta_1 + \beta_2)^2 + \beta_2(2\beta_1 + \beta_2)\Delta)}{32\omega_d^2} E^2 \bar{\phi}^2 - \frac{9(\alpha(\beta_1 + \beta_2)^2(\alpha + 2\Delta) + \beta_2(2\beta_1 + \beta_2)\Delta^2)}{128\omega_d^3} E^2 \bar{\phi}^2 \\
& + \frac{17(\alpha(\beta_1 + \beta_2)^2(\alpha^2 + 3\alpha\Delta + 3\Delta^2) + \beta_2(2\beta_1 + \beta_2)\Delta^3)}{512\omega_d^4} E^2 \bar{\phi}^2 - \frac{21\beta_2^2(7\beta_1^2 + 10\beta_1\beta_2 + 4\beta_2^2)}{512\omega_d^3} E^4 \bar{\phi}^4 \\
& + \frac{(\alpha\beta_2(313\beta_1 + 527\beta_2)(\beta_1 + \beta_2)^2 + 107\beta_2^2(7\beta_1^2 - 10\beta_1\beta_2 + 4\beta_2^2)\Delta)}{2048\omega_d^4} E^4 \bar{\phi}^4.
\end{aligned} \tag{F19}$$

To avoid detuned Rabi oscillations, the effective Hamiltonian should not contain any contributions proportional to $\hat{b}^\dagger \hat{b}$. This results in the resonance condition $\Delta + \delta_3(\Delta) = 0$ for subharmonic driving to fix Δ and by that ω_d .

For the present parameters, we realize that the large anharmonicity α suppresses leakage into the second excited state and therefore we truncate the effective model to a two-level system. Finally, the time evolution is well described by the zeroth-order contribution of the Magnus

expansion [50,73]:

$$\begin{aligned}
\hat{U}(0, t_{\text{pulse}}) &= \exp \left(-i \int_0^{t_{\text{pulse}}} dt \hat{H}_{\text{eff},3}(t) \right) \\
&= \exp(-it_{\text{pulse}} \Omega_3 \hat{\sigma}_x),
\end{aligned} \tag{F20}$$

with the effective Rabi rate

$$\begin{aligned}
\Omega_3 = & \frac{1}{t_{\text{pulse}}} \int_0^{t_{\text{pulse}}} dt E(t)^3 \left(-\frac{\beta_1(6\alpha(\beta_1 + \beta_2)^2)}{768\omega_d^3} + \frac{\beta_1(6\alpha(\beta_1 + \beta_2)^2(\alpha + 3\Delta))}{3072\omega_d^4} \right) \bar{\phi}^3 \\
& + \frac{1}{t_{\text{pulse}}} \int_0^{t_{\text{pulse}}} dt E(t)^3 \left(\frac{\beta_1\beta_2(2\beta_1 + \beta_2)}{32\omega_d^2} - \frac{13\beta_1\beta_2(2\beta_1 + \beta_2)\Delta}{768\omega_d^3} + \frac{29\beta_1\beta_2(2\beta_1 + \beta_2)\Delta^2}{3072\omega_d^4} \right) \bar{\phi}^3 \\
& + \frac{1}{t_{\text{pulse}}} \int_0^{t_{\text{pulse}}} dt E(t)^5 \frac{\beta_1\beta_2^2(29\beta_1^2 + 38\beta_1\beta_2 + 14\beta_2^2)}{1024\omega_d^4} \bar{\phi}^5.
\end{aligned} \tag{F21}$$

From the structure of the commutators in Eq. (F13) which contribute to the Rabi rate, it becomes obvious that only odd powers of ϕ can contribute, with the lowest power possible being ϕ^n for an n -photon drive. Higher powers in drive amplitude exist as well, $\Omega_n \sim c_1 \bar{\phi}^n + c_2 \bar{\phi}^{n+2} + \dots$; however, the convergence of the power series in the experimental-parameter regime results in less dominant prefactors for larger powers in ϕ . In total, the Rabi frequency scales polynomially with the drive power, which matches the experimental data of Fig. 3.

APPENDIX G: TUNE-UP

To tune up the subharmonic gates, we track the qubit frequency with a local oscillator set at a fraction of the qubit frequency ω_{eg}/n , where n is the photon number of the subharmonic used for driving. Translating between the X and Y drives therefore requires changing the pulse phase by $\pi/2n$, as opposed to $\pi/2$ for on-resonance driving. As the qubit frequency is shifted upward during driving (see Fig. 2), a phase shift between the qubit rotating frame and the local oscillator of the arbitrary waveform generator

(AWG) arises, which is described by

$$\Delta\varphi = \frac{1}{n} \int_0^{t_{\text{pulse}}} \Delta\omega_{\text{eg}}(t) dt, \quad (\text{G1})$$

for a pulse length t_{pulse} . Here, the shift in qubit frequency $\Delta\omega_{\text{eg}}(t)$ includes the varying pulse amplitude over time, i.e., it includes ring-up and ring-down of the pulse. The prefactor $1/n$ in Eq. (G1) copes with setting the local oscillator of the AWG at ω_{eg}/n to ensure a consistent phase relation between the local oscillator and the rotating frame of the qubit. We correct for the total phase shift in Eq. (G1) acquired during a subharmonic gate by shifting the phase of consecutive pulses by $\Delta\varphi$, which is equivalent to a virtual- Z rotation.

Each pulse parameter is calibrated using a two-step tune-up procedure, comprising a rough calibration pass [see Figs. 9(a)–9(d)] and a fine calibration pass [see Figs. 9(e)–9(h)]. We denote gates gate applied to the qubit by $R_i(\theta)$, with the rotation angle θ induced around a given axis $i \in \{x, y, z\}$. First, the pulse length is calibrated with a Rabi experiment while sweeping the pulse time, followed

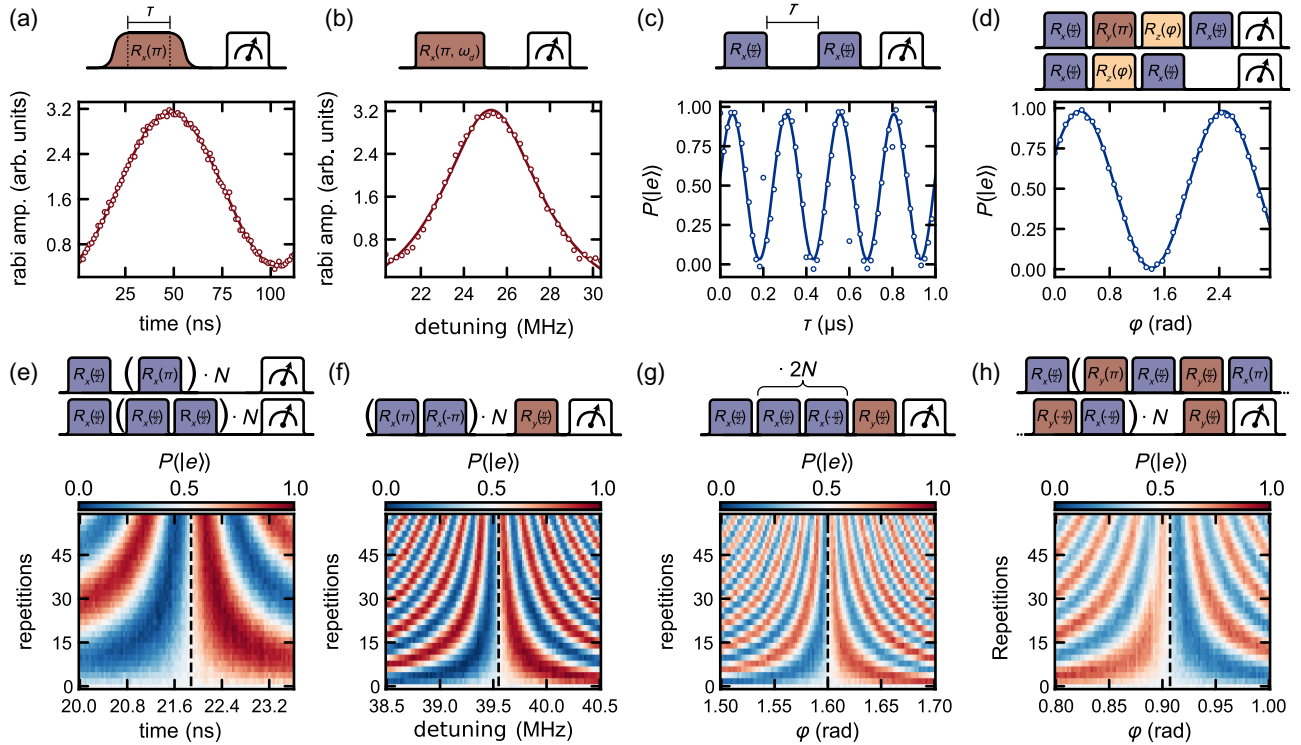


FIG. 9. The tune-up routine for single-qubit gates. The pulse is first (a)–(d) rough calibrated and subsequently (e)–(h) fine calibrated using error-amplification sequences, using different pulse sequences and subsequent measurement of the excited-state population. The pulse duration and detuning from ω_{eg}/n are calibrated with a Rabi experiment, changing the (a) time and (b) frequency of the drive pulse. (c) The qubit frequency is calibrated using a Ramsey experiment. (d) Calibration of the added pulse phase is performed separately for π and $\pi/2$ gates, also using a Ramsey-type experiment with an additional virtual- Z rotation before the second $\pi/2$ gate. (e)–(h) The error-amplification sequences shown are for (e) the pulse amplitude, (f) the frequency, (g) the $\pi/2$ -pulse phase, and (h) the π -pulse phase.

by a frequency calibration with a Rabi experiment, sweeping the pulse frequency instead. To increase the precision of the calibration, both steps are repeated multiple times until ω_d converges. These two steps are used to obtain the data shown in Figs. 2(d) and 3(b). Subsequently, the qubit frequency ω_{eg} while idling is calibrated using a Ramsey pulse sequence. To correct the additional phase added by the π and $\pi/2$ pulses, it is calibrated separately using a Ramsey-type sequence. Starting with the $\pi/2$ pulse, a Ramsey sequence with zero wait time and a virtual-Z rotation with a variable phase φ before the second pulse is used for the calibration. Finding the qubit in its excited state $P(|e\rangle) = 1$ determines the correct value of the compensation phase φ . To calibrate the π pulse, an $R_y(\pi)$ rotation is inserted into the Ramsey sequence, making it sensitive to the added phase of the π pulse. In this configuration, the sequence is insensitive to the amplitude of the π pulse and the virtual-Z gate again compensates the added phase correctly $P(|e\rangle) = 1$. Following the rough calibration, error-amplification sequences are performed to iteratively fine tune each pulse parameter. Each sequence keeps the qubit at an excited-state population of 0.5 for a perfectly calibrated pulse. Deviating from the optimal pulse parameter causes the excited-state population to oscillate, where the oscillation frequency indicates the magnitude of the error and the oscillation phase indicates the sign of the error. First, an $R_x(\pi/2)$ pulse, followed by N sequences of $R_x(\pi)$ or $2N$ sequences of $R_x(\pi/2)$ pulses for π and $\pi/2$ pulses, respectively [74], amplifies the over- and under-rotation error, which is corrected by optimizing the pulse length. Note that the AWG has a sampling time of $t_s = 0.5$ ns, necessitating a pulse duration of multiples of t_s and setting an upper bound on the precision of the gate. This limitation is circumvented by allowing the duration of the pulse shape to change independently of the sampling rate and filling the remaining time to the next sample with a zero-amplitude pulse, greatly increasing the pulse flexibility. Next, the frequency of the pulse is fine tuned using a phase-sensitive error-amplification sequence consisting of N consecutive $R_x(\pi)$ and $R_x(-\pi)$ rotation pairs [55]. After frequency calibration, the fine time-calibration steps are repeated. Finally, the phase of the $\pi/2$ and π pulse is calibrated with a sequence amplifying the error of the virtual-Z rotation [74]. In the sequence for the π pulse, the qubit is first prepared on the equator of the Bloch sphere using a $R_x(\pi/2)$ rotation, followed by a $R(\pi)$ rotation perpendicular to the prepared state, followed by another $R_x(\pi/2)$ rotation. This sequence is repeated for R_y rotations and in total repeated N times. Note that sequence shown in Figs. 9(f), used for calibrating the pulse frequency, is sensitive to changes in the phase shift of the virtual-Z gate. Therefore, the calibration routine must be executed in the exact order presented to avoid circular dependencies. In total, starting from an uncalibrated pulse, the tune-up process is completed within 10 min.

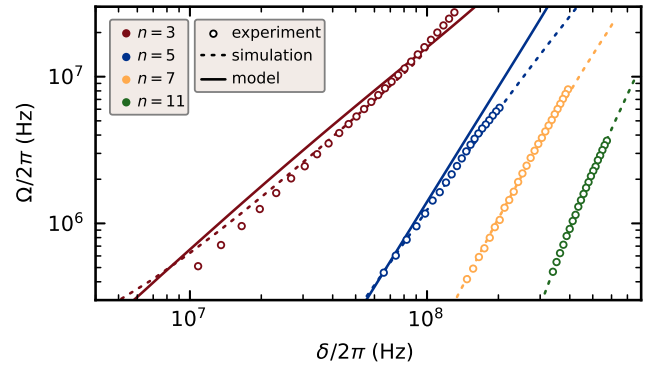


FIG. 10. The frequency shifts δ and Rabi frequencies Ω for the n th subharmonics: the Rabi frequencies as a function of drive-induced frequency shifts, as obtained from the theoretical model, numerical simulations, and experimental data. The expected dependence of $\Omega(\delta)$ (solid lines) from theory shows good agreement with the third subharmonic. The measurement errors are within the symbol size.

APPENDIX H: DRIVE-AMPLITUDE DISTORTION

Due to the long signal path from the room-temperature control electronics into the dilution cryostat, the microwave signals are attenuated and distorted, making it challenging to determine the exact drive power at the qubit. This distortion is given by the frequency-dependent transfer function of the signal line as a direct cause of impedance mismatches and the skin effect in the cables [51]. However, we find that for a subharmonic n , the drive-induced frequency shift δ and therefore the on-resonance drive frequency $\omega_d = (1/n)(\omega_{eg} + \delta_n)$ are direct measures of the applied drive power. In Fig. 10, we compare experimentally obtained Rabi frequencies versus the drive-induced frequency shift for different subharmonics with numerical simulations and theoretical predictions. Both the simulations and our model agree well with the experiments, strengthening our conclusion in Sec. IV that the transfer of the signal is the primary cause for deviations between theory and experiment. We also note that in comparing simulated versus measured frequency shifts as a function of the applied power, one can extract the frequency-domain transfer function of the flux line at the qubit.

-
- [1] S. Krinner, N. Lacroix, A. Remm, A. Di Paolo, E. Genois, C. Leroux, C. Hellings, S. Lazar, F. Swiadek, J. Herrmann, G. J. Norris, C. K. Andersen, M. Müller, A. Blais, C. Eichler, and A. Wallraff, Realizing repeated quantum error correction in a distance-three surface code, *Nature* **605**, 669 (2022).
 - [2] Google Quantum AI, Suppressing quantum errors by scaling a surface code logical qubit, *Nature* **614**, 676 (2023).
 - [3] V. V. Sivak, A. Eickbusch, B. Royer, S. Singh, I. Tsioutsios, S. Ganjam, A. Miano, B. L. Brock, A. Z. Ding, L. Frunzio,

- S. M. Girvin, R. J. Schoelkopf, and M. H. Devoret, Real-time quantum error correction beyond break-even, *Nature* **616**, 50 (2023).
- [4] J. Koch, T. M. Yu, J. Gambetta, A. A. Houck, D. I. Schuster, J. Majer, A. Blais, M. H. Devoret, S. M. Girvin, and R. J. Schoelkopf, Charge-insensitive qubit design derived from the Cooper pair box, *Phys. Rev. A* **76**, 042319 (2007).
- [5] Y. Kim, A. Eddins, S. Anand, K. X. Wei, E. van den Berg, S. Rosenblatt, H. Nayfeh, Y. Wu, M. Zaletel, K. Temme, and A. Kandala, Evidence for the utility of quantum computing before fault tolerance, *Nature* **618**, 500 (2023).
- [6] J. Lisenfeld, A. Bilmes, A. Megrant, R. Barends, J. Kelly, P. Klimov, G. Weiss, J. M. Martinis, and A. V. Ustinov, Electric field spectroscopy of material defects in transmon qubits, *npj Quantum Inf.* **5**, 1 (2019).
- [7] A. Gyenis, A. Di Paolo, J. Koch, A. Blais, A. A. Houck, and D. I. Schuster, Moving beyond the transmon: Noise-protected superconducting quantum circuits, *PRX Quantum* **2**, 030101 (2021).
- [8] J. Gao, Ph.D. thesis, Engineering and Applied Science, California Institute of Technology, 2008.
- [9] S. E. de Graaf, A. A. Adamyan, T. Lindström, D. Erts, S. E. Kubatkin, A. Ya. Tzalenchuk, and A. V. Danilov, Direct identification of dilute surface spins on Al_2O_3 : Origin of flux noise in quantum circuits, *Phys. Rev. Lett.* **118**, 057703 (2017).
- [10] M. Spiecker, P. Paluch, N. Gosling, N. Drucker, S. Matityahu, D. Gusenkova, S. Günzler, D. Rieger, I. Takmakov, F. Valenti, P. Winkel, R. Gebauer, O. Sander, G. Catelani, A. Shnirman, A. V. Ustinov, W. Wernsdorfer, Y. Cohen, and I. M. Pop, Two-level system hyperpolarization using a quantum Szilard engine, *Nat. Phys.* **19**, 1320 (2023).
- [11] C. Wang, C. Axline, Y. Y. Gao, T. Brecht, Y. Chu, L. Frunzio, M. H. Devoret, and R. J. Schoelkopf, Surface participation and dielectric loss in superconducting qubits, *Appl. Phys. Lett.* **107**, 162601 (2015).
- [12] K. D. Crowley, R. A. McLellan, A. Dutta, N. Shumiya, A. P. M. Place, X. H. Le, Y. Gang, T. Madhavan, M. P. Bland, R. Chang, N. Khedkar, Y. C. Feng, E. A. Umbarkar, X. Gui, L. V. H. Rodgers, Y. Jia, M. M. Feldman, S. A. Lyon, M. Liu, R. J. Cava, A. A. Houck, and N. P. de Leon, Disentangling losses in tantalum superconducting circuits, *Phys. Rev. X* **13**, 041005 (2023).
- [13] A. Somoroff, Q. Ficheux, R. A. Mencia, H. Xiong, R. Kuzmin, and V. E. Manucharyan, Millisecond coherence in a superconducting qubit, *Phys. Rev. Lett.* **130**, 267001 (2023).
- [14] V. E. Manucharyan, J. Koch, L. I. Glazman, and M. H. Devoret, Fluxonium: Single Cooper-pair circuit free of charge offsets, *Science* **326**, 113 (2009).
- [15] F. Wang, K. Lu, H. Zhan, L. Ma, F. Wu, H. Sun, H. Deng, Y. Bai, F. Bao, X. Chang, R. Gao, X. Gao, G. Gong, L. Hu, R. Hu, H. Ji, X. Ma, L. Mao, Z. Song, C. Tang, H. Wang, T. Wang, Z. Wang, T. Xia, H. Xu, Z. Zhan, G. Zhang, T. Zhou, M. Zhu, Q. Zhu, S. Zhu, X. Zhu, Y. Shi, H.-H. Zhao, and C. Deng, High-coherence fluxonium qubits manufactured with a wafer-scale-uniformity process, *Phys. Rev. Appl.* **23**, 044064 (2025).
- [16] L. Ding, M. Hays, Y. Sung, B. Kannan, J. An, A. Di Paolo, A. H. Karamlou, T. M. Hazard, K. Azar, D. K. Kim, B. M. Niedzielski, A. Melville, M. E. Schwartz, J. L. Yoder, T. P. Orlando, S. Gustavsson, J. A. Grover, K. Serniak, and W. D. Oliver, High-fidelity, frequency-flexible two-qubit fluxonium gates with a transmon coupler, *Phys. Rev. X* **13**, 031035 (2023).
- [17] Y.-H. Lin, L. B. Nguyen, N. Grabon, J. San Miguel, N. Pankratova, and V. E. Manucharyan, Demonstration of protection of a superconducting qubit from energy decay, *Phys. Rev. Lett.* **120**, 150503 (2018).
- [18] I. N. Moskalenko, I. A. Simakov, N. N. Abramov, A. A. Grigorev, D. O. Moskalev, A. A. Pishchimova, N. S. Smirnov, E. V. Zikiy, I. A. Rodionov, and I. S. Besedin, High fidelity two-qubit gates on fluxoniums using a tunable coupler, *npj Quantum Inf.* **8**, 1 (2022).
- [19] H. Zhang, C. Ding, D. Weiss, Z. Huang, Y. Ma, C. Guinn, S. Sussman, S. P. Chitta, D. Chen, A. A. Houck, J. Koch, and D. I. Schuster, Tunable inductive coupler for high-fidelity gates between fluxonium qubits, *PRX Quantum* **5**, 020326 (2024).
- [20] L. B. Nguyen, G. Koolstra, Y. Kim, A. Morvan, T. Chistolini, S. Singh, K. N. Nesterov, C. Jünger, L. Chen, Z. Pedramrazi, B. K. Mitchell, J. M. Kreikebaum, S. Puri, D. I. Santiago, and I. Siddiqi, Blueprint for a high-performance fluxonium quantum processor, *PRX Quantum* **3**, 037001 (2022).
- [21] A. A. Houck, J. A. Schreier, B. R. Johnson, J. M. Chow, J. Koch, J. M. Gambetta, D. I. Schuster, L. Frunzio, M. H. Devoret, S. M. Girvin, and R. J. Schoelkopf, Controlling the spontaneous emission of a superconducting transmon qubit, *Phys. Rev. Lett.* **101**, 080502 (2008).
- [22] R. J. Schoelkopf, A. A. Clerk, S. M. Girvin, K. W. Lehnert, and M. H. Devoret, in *Quantum Noise in Mesoscopic Physics*, edited by Y. V. Nazarov (Springer Netherlands, Dordrecht, 2003), pp. 175–203.
- [23] S. Krinner, S. Storz, P. Kurpiers, P. Magnard, J. Heinsoo, R. Keller, J. Lütolf, C. Eichler, and A. Wallraff, Engineering cryogenic setups for 100-qubit scale superconducting circuit systems, *EPJ Quantum Technol.* **6**, 2 (2019).
- [24] F. Yan, S. Gustavsson, A. Kamal, J. Birenbaum, A. P. Sears, D. Hover, T. J. Gudmundsen, D. Rosenberg, G. Samach, S. Weber, J. L. Yoder, T. P. Orlando, J. Clarke, A. J. Kerman, and W. D. Oliver, The flux qubit revisited to enhance coherence and reproducibility, *Nat. Commun.* **7**, 12964 (2016).
- [25] S. Kono, K. Koshino, D. Lachance-Quirion, A. F. van Loo, Y. Tabuchi, A. Noguchi, and Y. Nakamura, Breaking the trade-off between fast control and long lifetime of a superconducting qubit, *Nat. Commun.* **11**, 3683 (2020).
- [26] J. H. Shirley, Solution of the Schrödinger equation with a Hamiltonian periodic in time, *Phys. Rev.* **138**, B979 (1965).
- [27] M. Ferray, A. L’Huillier, X. F. Li, L. A. Lompre, G. Mainfray, and C. Manus, Multiple-harmonic conversion of 1064 nm radiation in rare gases, *J. Phys. B: At., Mol. Opt. Phys.* **21**, L31 (1988).
- [28] A. McPherson, G. Gibson, H. Jara, U. Johann, T. S. Luk, I. A. McIntyre, K. Boyer, and C. K. Rhodes, Studies of multiphoton production of vacuum-ultraviolet radiation in the rare gases, *J. Opt. Soc. Am. B* **4**, 595 (1987).
- [29] Y. Nakamura, Yu. A. Pashkin, and J. S. Tsai, Rabi oscillations in a Josephson-junction charge two-level system, *Phys. Rev. Lett.* **87**, 246601 (2001).

- [30] A. Wallraff, T. Duty, A. Lukashenko, and A. V. Ustinov, Multiphoton transitions between energy levels in a current-biased Josephson tunnel junction, *Phys. Rev. Lett.* **90**, 037003 (2003).
- [31] S. Saito, M. Thorwart, H. Tanaka, M. Ueda, H. Nakano, K. Semba, and H. Takayanagi, Multiphoton transitions in a macroscopic quantum two-state system, *Phys. Rev. Lett.* **93**, 037001 (2004).
- [32] C. Liu, A. Ballard, D. Olaya, D. Schmidt, J. Biesecker, T. Lucas, J. Ullom, S. Patel, O. Rafferty, A. Opremcak, K. Dodge, V. Iaia, T. McBroom, J. DuBois, P. Hopkins, S. Benz, B. Plourde, and R. McDermott, Single flux quantum-based digital control of superconducting qubits in a multichip module, *PRX Quantum* **4**, 030310 (2023).
- [33] M. Xia, C. Zhou, C. Liu, P. Patel, X. Cao, P. Lu, B. Mesits, M. Mucci, D. Gorski, D. Pekker, and M. Hatridge, Fast superconducting qubit control with sub-harmonic drives, [ArXiv:2306.10162](https://arxiv.org/abs/2306.10162) [quant-ph].
- [34] A. Sah, S. Kundu, H. Suominen, Q. Chen, and M. Möttönen, Decay-protected superconducting qubit with fast control enabled by integrated on-chip filters, *Commun. Phys.* **7**, 227 (2024).
- [35] D. A. Rower, L. Ding, H. Zhang, M. Hays, J. An, P. M. Harrington, I. T. Rosen, J. M. Gertler, T. M. Hazard, B. M. Niedzielski, M. E. Schwartz, S. Gustavsson, K. Serniak, J. A. Grover, and W. D. Oliver, Suppressing counter-rotating errors for fast single-qubit gates with fluxonium, *PRX Quantum* **5**, 040342 (2024).
- [36] I. M. Pop, K. Geerlings, G. Catelani, R. J. Schoelkopf, L. I. Glazman, and M. H. Devoret, Coherent suppression of electromagnetic dissipation due to superconducting quasiparticles, *Nature* **508**, 369 (2014).
- [37] H. Nyquist, Thermal agitation of electric charge in conductors, *Phys. Rev.* **32**, 110 (1928).
- [38] M. Reed, Ph.D. thesis, Physics Department, Yale University, Yale, 2013.
- [39] A. Gyenis, P. S. Mundada, A. Di Paolo, T. M. Hazard, X. You, D. I. Schuster, J. Koch, A. Blais, and A. A. Houck, Experimental realization of a protected superconducting circuit derived from the $0-\pi$ qubit, *PRX Quantum* **2**, 010339 (2021).
- [40] F. Hassani, M. Peruzzo, L. N. Kapoor, A. Trioni, M. Zemlicka, and J. M. Fink, Inductively shunted transmons exhibit noise insensitive plasmon states and a fluxon decay exceeding 3 hours, *Nat. Commun.* **14**, 3968 (2023).
- [41] E. M. Purcell, H. C. Torrey, and R. V. Pound, Resonance absorption by nuclear magnetic moments in a solid, *Phys. Rev.* **69**, 37 (1946).
- [42] X. You, J. A. Sauls, and J. Koch, Circuit quantization in the presence of time-dependent external flux, *Phys. Rev. B* **99**, 174512 (2019).
- [43] A. Blais, A. L. Grimsmo, S. M. Girvin, and A. Wallraff, Circuit quantum electrodynamics, *Rev. Mod. Phys.* **93**, 025005 (2021).
- [44] F. Yan, S. Gustavsson, J. Bylander, X. Jin, F. Yoshihara, D. G. Cory, Y. Nakamura, T. P. Orlando, and W. D. Oliver, Rotating-frame relaxation as a noise spectrum analyser of a superconducting qubit undergoing driven evolution, *Nat. Commun.* **4**, 2337 (2013).
- [45] W. Ardati, S. Léger, S. Kumar, V. N. Suresh, D. Nicolas, C. Mori, F. D'Esposito, T. Vakhtel, O. Buisson, Q. Ficheux, and N. Roch, Using bifluxon tunneling to protect the fluxonium qubit, *Phys. Rev. X* **14**, 041014 (2024).
- [46] F. Yan, D. Campbell, P. Krantz, M. Kjaergaard, D. Kim, J. L. Yoder, D. Hover, A. Sears, A. J. Kerman, T. P. Orlando, S. Gustavsson, and W. D. Oliver, Distinguishing coherent and thermal photon noise in a circuit quantum electrodynamical system, *Phys. Rev. Lett.* **120**, 260504 (2018).
- [47] F. Pfeiffer, M. Werninghaus, C. Schweizer, N. Bruckmoser, L. Koch, N. J. Glaser, G. B. P. Huber, D. Bunch, F. X. Haslbeck, M. Knudsen, G. Krylov, K. Liegener, A. Marx, L. Richard, J. H. Romeiro, F. A. Roy, J. Schirk, C. Schneider, M. Singh, L. Södergren, I. Tsitsilin, F. Wallner, C. A. Riofrio, and S. Filipp, Efficient decoupling of a nonlinear qubit mode from its environment, *Phys. Rev. X* **14**, 041007 (2024).
- [48] C. Müller, J. H. Cole, and J. Lisenfeld, Towards understanding two-level-systems in amorphous solids: Insights from quantum circuits, *Rep. Prog. Phys.* **82**, 124501 (2019).
- [49] We emphasize that \hat{b}^\dagger and \hat{b} are not equal to the ladder operators of an LC oscillator, for which the flux operator can be expressed as $\hat{\varphi} \propto \hat{a} + \hat{a}^\dagger$. This approximation only holds for weakly anharmonic oscillators such as the transmon [43].
- [50] W. Magnus, On the exponential solution of differential equations for a linear operator, *Commun. Pure Appl. Math.* **7**, 649 (1954).
- [51] R. L. Wigington and N. S. Nahman, Transient analysis of coaxial cables considering skin effect, *Proc. IRE* **45**, 166 (1957).
- [52] W. Heinrich, Quasi-TEM description of mmic coplanar lines including conductor-loss effects, *IEEE Trans. Microw. Theory Tech.* **41**, 45 (1993).
- [53] M. A. Rol, L. Ciorcioaro, F. K. Malinowski, B. M. Tarasinski, R. E. Sagastizabal, C. C. Bultink, Y. Salathe, N. Haandbæk, J. Sedivy, and L. DiCarlo, Time-domain characterization and correction of on-chip distortion of control pulses in a quantum processor, *Appl. Phys. Lett.* **116**, 054001 (2020).
- [54] L. Huang, J. Luneau, S. Filipp, P. Rabl, and K. Liegener, Theory of multi-photon processes in subharmonically driven superconducting circuits, in preparation (2025).
- [55] J. M. Gambetta, F. Motzoi, S. T. Merkel, and F. K. Wilhelm, Analytic control methods for high-fidelity unitary operations in a weakly nonlinear oscillator, *Phys. Rev. A* **83**, 012308 (2011).
- [56] R. Barends, J. Kelly, A. Megrant, A. Veitia, D. Sank, E. Jeffrey, T. C. White, J. Mutus, A. G. Fowler, B. Campbell, Y. Chen, Z. Chen, B. Chiaro, A. Dunsworth, C. Neill, P. O'Malley, P. Roushan, A. Vainsencher, J. Wenner, A. N. Korotkov, A. N. Cleland, and J. M. Martinis, Superconducting quantum circuits at the surface code threshold for fault tolerance, *Nature* **508**, 500 (2014).
- [57] S. Lazăr, Q. Ficheux, J. Herrmann, A. Remm, N. Lacroix, C. Hellings, F. Swiadek, D. C. Zanuz, G. J. Norris, M. B. Panah, A. Flasby, M. Kerschbaum, J.-C. Besse, C. Eichler, and A. Wallraff, Calibration of drive nonlinearity for arbitrary-angle single-qubit gates using error amplification, *Phys. Rev. Appl.* **20**, 024036 (2023).

- [58] L. H. Pedersen, N. M. Møller, and K. Mølmer, Fidelity of quantum operations, *Phys. Lett. A* **367**, 47 (2007).
- [59] Z. Huang, P. S. Mundada, A. Gyenis, D. I. Schuster, A. A. Houck, and J. Koch, Engineering dynamical sweet spots to protect qubits from $1/f$ noise, *Phys. Rev. Appl.* **15**, 034065 (2021).
- [60] P. S. Mundada, A. Gyenis, Z. Huang, J. Koch, and A. A. Houck, Floquet-engineered enhancement of coherence times in a driven fluxonium qubit, *Phys. Rev. Appl.* **14**, 054033 (2020).
- [61] M. Werninghaus, D. J. Egger, F. Roy, S. Machnes, F. K. Wilhelm, and S. Filipp, Leakage reduction in fast superconducting qubit gates via optimal control, *npj Quantum Inf.* **7**, 1 (2021).
- [62] C. P. Koch, U. Boscain, T. Calarco, G. Dirr, S. Filipp, S. J. Glaser, R. Kosloff, S. Montangero, T. Schulte-Herbrüggen, D. Sugny, and F. K. Wilhelm, Quantum optimal control in quantum technologies. strategic report on current status, visions and goals for research in Europe, *EPJ Quantum Technol.* **9**, 19 (2022).
- [63] M. Brink, J. M. Chow, J. Hertzberg, E. Magesan, and S. Rosenblatt, in *2018 IEEE International Electron Devices Meeting (IEDM)* (IEEE, San Francisco, 2018), pp. 6.1.1–6.1.3.
- [64] J. Schirk, F. Wallner, C. Schneider, and S. Filipp, Supporting data for “Subharmonic Control of a Fluxonium Qubit via a Purcell-Protected Flux Line”, Zenodo, <https://doi.org/10.5281/zenodo.15841399> (2025).
- [65] I. N. Moskalenko, I. S. Besedin, I. A. Simakov, and A. V. Ustinov, Tunable coupling scheme for implementing two-qubit gates on fluxonium qubits, *Appl. Phys. Lett.* **119**, 194001 (2021).
- [66] P. Groszkowski and J. Koch, ScQubits: A PYTHON package for superconducting qubits, *Quantum* **5**, 583 (2021).
- [67] S. P. Chitta, T. Zhao, Z. Huang, I. Mondragon-Shem, and J. Koch, Computer-aided quantization and numerical analysis of superconducting circuits, *New J. Phys.* **24**, 103020 (2022).
- [68] P. Krantz, M. Kjaergaard, F. Yan, T. P. Orlando, S. Gustavsson, and W. D. Oliver, A quantum engineer’s guide to superconducting qubits, *Appl. Phys. Rev.* **6**, 021318 (2019).
- [69] A. A. Clerk and D. W. Utami, Using a qubit to measure photon-number statistics of a driven thermal oscillator, *Phys. Rev. A* **75**, 042302 (2007).
- [70] R. K. Pathria and P. D. Beale, *Statistical Mechanics* (Butterworth-Heinemann, 2011).
- [71] M. Khapaev, A. Kidiyarova-Shevchenko, P. Magnelind, and M. Kupriyanov, 3D-MLSI: Software package for inductance calculation in multilayer superconducting integrated circuits, *IEEE Trans. Appl. Supercond.* **11**, 1090 (2001).
- [72] N. Goldman, J. Dalibard, M. Aidelsburger, and N. R. Cooper, Periodically driven quantum matter: The case of resonant modulations, *Phys. Rev. A* **91**, 033632 (2015).
- [73] Note, that in principle this formulation would also allow to treat nontrivial envelope functions by computing higher orders in the Magnus expansion given that the envelope varies slowly enough compared to ω_d .
- [74] S. Sheldon, L. S. Bishop, E. Magesan, S. Filipp, J. M. Chow, and J. M. Gambetta, Characterizing errors on qubit operations via iterative randomized benchmarking, *Phys. Rev. A* **93**, 012301 (2016).